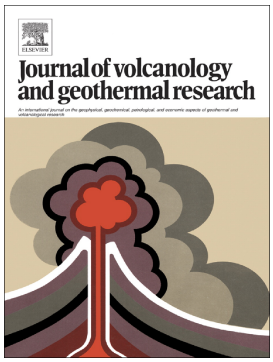

The 2011–2012 paroxysmal eruptions at Mt. Etna volcano: Insights on the vertically zoned plumbing system

P.P. Giacomoni, M. Coltorti, S. Mollo, C. Ferlito, M. Braiato, P. Scarlato

PII: S0377-0273(17)30464-X
DOI: doi:10.1016/j.jvolgeores.2017.11.023
Reference: VOLGEO 6250

To appear in: *Journal of Volcanology and Geothermal Research*

Received date: 31 July 2017
Revised date: 21 November 2017
Accepted date: 22 November 2017

Please cite this article as: P.P. Giacomoni, M. Coltorti, S. Mollo, C. Ferlito, M. Braiato, P. Scarlato , The 2011–2012 paroxysmal eruptions at Mt. Etna volcano: Insights on the vertically zoned plumbing system. The address for the corresponding author was captured as affiliation for all authors. Please check if appropriate. Volgeo(2017), doi:10.1016/j.jvolgeores.2017.11.023

The 2011-2012 paroxysmal eruptions at Mt. Etna volcano: Insights on the vertically zoned plumbing system

Giacomoni P.P.[1], Coltorti M.[1], Mollo S.[2], Ferlito C.[3], Braiato M.[1], Scarlato P.[4]

[1] Department of Physics and Earth Sciences, University of Ferrara, Italy

[2] Department of Earth Science, University of La Sapienza, Italy

[3] Department of Biological, Environmental and Geological Sciences, University of Catania, Italy

[4] HP-HT Laboratory, National Institute of Geophysics and Volcanology (INGV-Italy)

ABSTRACT

The activity of Mt. Etna volcano from January 2011 to April 2012 was characterized by 24 paroxysmal, short-duration (from a few to several hours) eruptions at the New South-East summit crater. Despite the violence of the activity, no appreciable geophysical signals were recorded during this period, except for an increase in seismic tremors just minutes/hours before the occurrence of the paroxysm. This type of activity represents a significant shift from the mainly effusive eruptions of 2004, 2006, and 2008/2009, as well as from the lateral rift-related events of 2001 and 2002/2003.

The 2011-2012 paroxysmal activity thus represents an important opportunity to better understand the effects of different magmatic parameters (i.e., *P-T-fO*$_2$) and magmatic H_2O content on the crystallization and fractionation processes. To this aim the petrographic and geochemical features of lava and scoria clasts from 10 paroxysmal events have been investigated. Fractional crystallization modelling indicates that most of the eruptions are related to magmas rising along the vertically-developed feeding system of the volcano, accompanied by one main recharge of a more primitive, deep-seated magma feeding the

4/3/2012 event. Olivine-, clinopyroxene-, and plagioclase-melt equilibria and thermobarometric calculations were performed in order to estimate the crystallization conditions of magmas. These calculations reveal that the erupted products contain different phenocryst populations in equilibrium with a spectrum of primitive to more evolved magma compositions. On the basis of crystal composition, crystal-melt equilibrium conditions and thermobarometric estimations, four main magmatic facies have been recognized: F1, 1600 MPa at 1270 °C (Ol Fo_{88}); F2, 800 MPa to 600 MPa at 1178 °C to 1151 °C (Ol Fo_{84-78}); F3, 450 MPa to 250 MPa at 1139 °C to 1118 °C (Ol Fo_{79-74}); F4, <250 MPa at <1120 °C (Ol Fo_{75-70}). The overall geochemistry and thermobarometric data allow us to characterize the central feeding system as continuous and vertically zoned. During the 2011-2012 activity the studied 30/7/11, 29/8/11, 8/9/11, 18/3/11 and 24/4/12 events were fed by magma residing at F3 and F4 facies. Mafic magma influx from deeper F2 facies occurred ~~the~~ 18/2/11 and 20/8/11, with a major recharge event before the 4/3/12 eruption. The primitive magma is testified by rare olivine crystals equilibrated at the F1 facies, located at crust-mantle boundary depth and close to liquidus temperature.

INTRODUCTION

Because of its variable and persistent volcanic activity, Mt. Etna (Sicily, Italy) represents a natural laboratory for studying the magmatic processes that control the nucleation and growth of phenocrysts during magma ascent from depth to eruption at the surface (Armienti *et al*., 2012; Giacomoni *et al.,* 2014; Giacomoni *et al.,* 2016; Mollo *et al*. 2015a).

Volcanological, geophysical and petrological studies highlighted three main volcanic feeding systems responsible for the historical eruptive event: the central conduit feeding system, persistently filled with magma from which degassing feeds fumarole activity at the summit

craters; the lateral feeding systems (S-Rift, NE-Rift and the W-Rift); and the eccentric feeding system (Kieffer, 1975).

In such a complex volcanological setting, recent studies have discovered a variety of crystallization scenarios, recorded in textural variations and chemical zoning of olivine (Khal *et al.*, 2011; Mollo *et al.,* 2015a), clinopyroxene (Mollo *et al.,* 2015b; Giacomoni *et al.,* 2016), plagioclase (Viccaro *et al.,* 2010; Giacomoni *et al.,* 2014) and Ti-magnetite (Mollo *et al.,* 2015b). These phenocrysts record a wide range of mineral-melt equilibration conditions, from early nucleation and growth at mantle depths (i.e., olivine and clinopyroxene) to magma conduit dynamics, where assimilation, fractional crystallization, and magma mixing phenomena occur.

In the last 20 years, the volcanic activity of Mt. Etna displayed a great variety of eruptive styles, from long lasting effusive events with minor strombolian activity and scarce seismic precursors (2004, 2006, and 2008/2009 eruptions; Di Grazia *et al.,* 2006; Andronico *et al.,* 2008; Aloisi *et al.,* 2009; Corsaro *et al.*, 2009; Aiuppa *et al.,* 2010) to explosive events from extended fractures on the flanks of the edifice, often preceded by intense seismic activity (2001, and 2002/2003 eruptions; Behncke *et al.,* 2003; Andronico *et al.*, 2005).

The eruptive events that occurred from January 12th 2011 to April 24th 2012 represent, however, a radical shift in the eruptive style. Indeed, within a short time interval, 25 summit paroxysmal episodes were observed at the New South-East Crater (NSEC). These eruptions consisted of sustained jets of magma and gas (reaching up to 800 m in height) and were defined as lava fountains for their frequency and type of activity (Calvari *et al.*, 2011; Bonaccorso *et al.,* 2013). These latter events are associated with short-lasting lava flows, usually flowing down into the Valle del Bove (Fig. 1) and covering an overall area of 3.19 km^2 for a maximum length of 4.3 km (Behncke *et al.*, 2014; Viccaro *et al.,* 2015). Despite the violence of the activity, no appreciable geophysical signals were recorded during this period,

except for an increase in seismic tremors just a few minutes/hours before the occurrence of the paroxysm (Bonaccorso *et al.,* 2013).

This eruptive sequence and its associated products give us the opportunity to investigate the mechanisms of magma ascent, degassing, and crystallization along the magma column residing in the central volcanic conduit, as well as to better understand the physicochemical changes of the system that caused the unexpected and violent eruptive activity of the volcano. In this context, lava and tephra from ten events (from Feb 18th 2011 to Apr 24th 2012) have been investigated a petrographically, mineralogically, and geochemically. The recovered information has been then used to model magmatic differentiation and the recharging mechanisms responsible for the eruptive events.

GEOLOGICAL BACKGROUND

Mt. Etna is a 3340 m a.s.l. high stratovolcano located on the eastern coast of Sicily (Fig. 1a). Magmatic activity started ~500 ka ago with the emission of olivine tholeiitic basalts, accompanied by a few pigeonite-bearing tholeiitic basalts from fissural submarine and subaerial vents (Gillot *et al.,* 1994; Tanguy *et al.,* 1997). The early submarine volcanic events were followed by subaerial eruptions, in concert with a regional uplifting that occurred ~300 ka ago (Branca *et al.,* 2008). The composition of the erupted products shifted from tholeiitic to transitional to Na-alkalic (~200 ka; Tanguy *et al.,* 1997 and references therein). The building of central-conduit edifice started ~130 ka ago, resulting in a sequence of several distinct volcanic centers characterized by alternation of effusive and explosive eruptions and frequently associated with caldera collapses (De Beni *et al.,* 2005). The "Recent Mongibello" activity initiated ~15 ka ago, being predominantly effusive with lava emissions and strombolian eruptions from the summit craters and/or from eccentric parasitic cones forming at the volcanic flanks (Branca *et al.,* 2008).

The present feeding system is interpreted as an open-conduit system developed at the intersection of two main volcano-tectonic structures: the North East Rift and the South Rift (Ferlito *et al.,* 2009; Giacomoni *et al.,* 2012), which are strictly related to the trans-extensional regional tectonic regime (Monaco *et al.,* 2005). The main volcanic conduit is persistently filled with magma at different levels, which undergoes continuous degassing from the summit craters (Corsaro *et al.,* 2009).

Recent petrological (Kahl *et al.,* 2011; Kahl *et al.,* 2013; Giacomoni *et al.,* 2016) and geophysical (Patanè *et al.,* 2006; Patanè *et al.,* 2013) studies describe the Etnean feeding system as continuous, from mantle depth to the surface, without long-persisting magma chambers, but often characterized by preferential magma ponding zones located at depths corresponding to the main crustal discontinuities with a significant overlap. Three main ponding levels have been recognized: 1) at the mantle/crust interface corresponding to the Moho discontinuity at ~27 km b.s.l. (Sharp *et al.,* 1980), 2) inside the Mesozoic carbonate succession at ~4-8 km b.s.l. (Lundgren *et al.,* 2003), and 3) inside the Appennine-Maghrebian formations at ~3-6 km (Bonaccorso et al., 2011).

DESCRIPTION OF THE 2011-2012 PAROXISMAL ERUPTIONS

From January 2011 to April 2012, twenty-five eruptive episodes were recorded and described in the monitoring reports of the Istituto Nazionale di Geofisica e Vulcanologia (INGV), including direct observations and geophysical data collected from permanent monitoring stations (Table 1).

The volcanic activity occurred from the New South-East Crater (NSEC), which is a 300-m-high scoria cone with a volume of approximately 19×10^6 m^3. This cone was generated by the accumulation of pyroclastic material ejected from a pit crater formed after the 16th November 2006 flank collapse of the South-East Crater (SEC) (Ferlito *et al.,* 2010; Neri *et al.,* 2010).

The eruptive events were characterized by violent strombolian explosions and sustained lava fountaining with a maximum height of 800 m and time duration from a few hours to a few days. Lava flows outpoured from the eastern flank of the NSEC with low emission rates and moved southeastward into the Valle Del Bove, while frequent and intense ash plumes drifted with dominant winds towards the city of Catania.

The eruptive events investigated in this study occurred on 18th February 2011, 10th April 2011, 12th May 2011, 30th July 2011, 20th August 2011, 29th August 2011, 8th September 2011, 4th March 2012, 18th March 2012, and 24th April 2012. Overall, ten eruptive events have been analyzed and hereafter labelled as 18/2/2011, 10/4/2011, 12/5/2011, 30/7/2011, 20/8/2011, 29/8/2011, 8/9/2011, 4/3/2012, 18/3/2012 and 24/4/2012.

The 18/2/2011 volcanic activity started at 1.15 GMT (Fig. 1b) and was characterized by intense degassing from the SEC. After ~2 h, increasing seismic tremor (M<2) was followed by explosions indicating the beginning of the eruption. Due to cloudy weather conditions, only a small portion of the lava flow was visible, outpouring from the SEC western flank. The 10/4/2011 and 12/5/2011 eruptions (Figs. 1c and d) started at 9.30 GMT and 4.00 GMT, respectively, as lava fountaining ejected from the low topographic sectors of the SEC. These explosive events produced ash clouds that was wind-driven south-southeastward. The 12/5/2011 lava fountain started in the night at the SEC and was accompanied by an ash cloud that was blown south-southeastward. Afterwards, a lava flow outpoured from the SEC east flank and flowed eastward in the Valle Del Bove (Fig. 1d). Before the 30/7/2011 event, a minimum of three eruptions were reported by the INGV: 9/7/2011, 19/7/2011, and 24/7/2011 none of which could be sampled (Table 1). The 30/7/2011 event (Fig. 1e) began at the 19.30 GMT and was preceded by intermittent and sporadic strombolian explosions two days before. These explosions were characterized by increasing intensity and frequency, and were

accompanied by an eastward-directed ash fall. The energy of the explosions faded after ~2 h, and the strombolian activity was concluded at 22.00 GMT.

From 30th July 2011 to 30th August 2011, the INGV reports also two explosive events labelled 5/8/2011 and 12/8/2011 (Table 1). On 20th August 2011, an increase in tremor with subsequent strombolian explosions (Fig. 1f) was recorded at 2.30 GMT. Afterwards, the intensity and frequency of the tremor substantially increased and the volcanic activity shifted to lava fountaining with the formation of an eruptive column. Different from previous eruptive events, this latter was fed by two different vents located at the south-east flank of SEC and identified by lava jets with height of ~100 m. The 29/8/2011 eruptions (Fig. 1g) were similar to those described above, with the exception of the collapse of the south-eastern sector of the SEC. The 8/9/2011 eruption (Fig. 1h) was anticipated by weak and sporadic strombolian explosions and reached its climax at 6.30 GMT with intermittent lava fountains, generating an eruption column. At 6.50 GMT, several landslides of unconsolidated pyroclastic material involved the unstable east flank of the cone formed at the SEC.

Before the 4/3/2012 event, INGV documented the occurrence of six explosive eruptions from the pit crater at the south-east flank of the NSEC (Table 1). The 4/3/2012 event started at 4.29 GMT (Fig. 1i), preceded by an increase of volcanic tremor and was characterized by strong strombolian explosions that grew in frequency and energy over time. These explosions were accompanied by lava overflow from a fissure formed on the south-eastern edge of the NSEC. The flow reached the base of the cone and then headed towards the western flank of the Valle del Bove. At 7.30 GMT, volcanic activity shifted to a sustained lava fountaining that increased in intensity and generated an eruptive column of ~5000 m in height. At 7.48 GMT, a new eruptive vent formed at the south-western flank of the NSEC cone, feeding a new lava flow, outpouring between SEC and NSEC. Several small pyroclastic flows were observed flowing northeastward at the northern flank of the NSEC. The interaction between the hot

lava and snow strata caused vaporization phenomena associated with low-scale southward pyroclastic flows travelling a few hundreds of meters. The snow and ice melting also caused a lahar that flowed towards the "Belvedere" monitoring station, located on the western side of the Valle del Bove.

On the 18th March 2012 (Table 1), several monitoring stations recorded an increase of tremor signal at 4.00 GMT, associated with recurrence of intracrateric strombolian explosions at the NSEC. At 7.45 GMT, the strombolian explosions changed to sustained lava fountain and one lava flow moved towards the eastern flank of Valle Del Bove with several branches that interacted with snow causing phreatomagmatic explosions and small lahars (Fig. 1j).

The 24/4/2012 paroxysm started in the evening. Similarly, to the previous eruptive events, this eruption was characterized by highly sustained lava fountains accompanied by a tephra eruptive column. Ash and lapilli fallout affected the NE sector of the volcano and several lava flows streamed towards the Valle del Bove, forming a complex lava field (Fig. 1k).

ANALYTICAL METHODS

Whole-rock geochemical analyses were carried out at the laboratory of the Department of Physics and Earth Science of the University of Ferrara (Italy) using powdered aliquots of lava and tephra. Major- and some trace- element (Ba, Ce, Cr, Nb, Nd, Rb, Sc, V, Zr) concentrations were measured by X-ray fluorescence (Thermo ARL Advant XP). Intensities were corrected for matrix effects using the method of Lachance & Trail (1966). Loss on ignition (L.O.I.) was determined by gravimetric method, assuming Fe_2O_3 as 15% FeO. Th, U, and REE concentrations were measured by inductively coupled plasma mass spectrometry (ICP-MS) on a VG Elemental Plasma Quad 2Plus instrument. The data reproducibility ranges between 0.9% and 7.9%. From a conservative point of view, it has been determined an accuracy of 10% and a detection limit of 10 ppb for Th, U and REE.

Microchemical and textural analyses were conducted at the HP-HT Laboratory of Experimental Volcanology and Geophysics of the Istituto Nazionale di Geofisica e Vulcanologia (INGV) in Rome, Italy. Chemical analyses were carried out with a JEOL-JXA8200 electron probe micro-analyzer (EPMA) equipped with five spectrometers. Data were collected by analysing the cores and rims of phenocrysts, and coexisting glasses located a few microns next to crystal edges. The analyses were performed using an accelerating voltage of 15 kV and a beam current of 10 nA. For crystals, the beam size was 1 μm with a counting time of 20 and 10 s on peaks and background, respectively. For glasses, a slightly defocused electron beam with a size of 3 μm was used with a counting time of 5 s on background and 15 s on peak. The following standards have been adopted for the various chemical elements: jadeite (Si and Na), corundum (Al), forsterite (Mg), andradite (Fe), rutile (Ti), orthoclase (K), barite (Ba), apatite (P), spessartine (Mn) and chromite (Cr). Sodium and potassium were analyzed first to mitigate alkali migration effects. The precision of the microprobe was measured through the analysis of well-characterized synthetic oxides and minerals. Data quality was ensured by analyzing the test materials as unknowns according to Iezzi *et al.* (2014). Based on counting statistics, analytical uncertainties relative to their reported concentrations indicate that the accuracy was better than 5%. Images were collected using the backscattered electron (BSE) mode of a field emission gun-scanning electron microscopy (FE-SEM) JEOL 6500F equipped with an energy-dispersive spectrometer (EDS) detector.

PETROGRAPHY

The eruptive products sampled consist of seven lavas and three scoriaceous lapilli, whose petrographic features are summarized in Table 2.

Samples are porphyritic, with porphyritic indexes (P.I., defined as percentage of phenocryst respect to the whole thin section area) ranges from 15 to 30%. Phenocrysts are embedded in a groundmass that varies from glassy to hyalopilitic. The percentage of vesicles (i.e., vesicularity) varies from 30% in lavas up to 60% in scoriaceous lapilli of 10/4/2011 eruption.

All products share a common phenocryst assemblage of olivine (10-30%), clinopyroxene (20-40%), plagioclase (25-60%) and magnetite (≤5%). Rare apatite is also found as accessory phase in the hyalopilitic groundmass. Olivine phenocrysts are euhedral, and vary in size from 0.5 to 2 mm. Large olivine often contains brownish, partially crystallized melt inclusions and oxides. Clinopyroxene is the most abundant femic mineral, varying in size from 0.7 to 4 mm, and plagioclase ranges in size from 200 μm to 3 mm.

WHOLE-ROCK GEOCHEMISTRY

Whole-rock major- and trace- element concentrations are reported in Table 3. The TAS (Total Alkali vs. Silica) diagram shows that the studied products vary from hawaiite (e.g. 10/4/2011) to mugearite (29/8/2011), with one trachybasalt (4/3/2012) (Fig. 2a), with SiO_2 and Na_2O+K_2O contents varying from 47.69 to 50.82 wt.% and from 5.67 to 6.66 wt.%, respectively.

The MgO vs. TiO_2, CaO, Na_2O, and K_2O diagrams (Fig. 2b) indicate that as TiO_2 (1.71 - 1.87 wt.%) and CaO (9.94 - 11.30 wt.%) decrease with differentiation, being positively correlated with MgO. In contrast, Na_2O (3.61-4.67 wt.%) and K_2O (1.97 to 2.17 wt.%) increase with decreasing MgO. Two distinct trends are observed for K_2O: the first occurs in a narrow range of MgO (4.1-4.5 wt.%), whereas the second develops along a wider MgO interval (4.2-5.5 wt.%).

Primordial mantle-normalized trace- element diagrams (McDonough & Sun (1995) compare well with the typical intraplate Etnean pattern (Peccerillo, 2005; Ferlito *et al.,* 2009; Schiavi

et al., 2015), characterized by general enrichment in incompatible elements with negative anomalies in Rb, Ta, Hf, Ti and slightly negative K anomaly to respect to La (Fig. 3). The absence of Eu negative anomaly suggests that plagioclase fractionation occurred during late differentiation at low pressure conditions.

MINERAL AND GLASS CHEMISTRY

Major element compositions of mineral phases and matrix glass are reported in the supplementary online material. Olivine has a wide range of compositions that can be categorized into four groups on the basis of forsterite (Fo) content: M_M (Fo = 0.88); M_0 (Fo = 0.84 - 0.77); M_1 (Fo = 0.79 - 0.77); M_2 (Fo = 0.75 - 0.7). As will be discussed in the following, M_0, M_1 and M_2 groups often coexist in the same sample in variable proportions, whereas olivine phenocrysts with M_M composition are rare and found exclusively in 18/2/11 products.

The majority of clinopyroxene phenocrysts are augites (Morimoto, 1988), with Mg# (Mg#= atomic Mg/Mg+Fe^{2+} where Fe^{2+} is calculated as total iron) between 71 and 78; CaO varies from 21.4 wt.% to 23 wt.% and TiO_2 ranging from 0.85 wt.% to 3.4 wt.% (Fig. 4a). Clinopyroxene phenocrysts from the 8/9/2011 eruption are euhedral (Fig. 4b) with homogeneous compositions (Mg# 75-77). Conversely, despite euhedral shapes, phenocrysts from the 4/3/2012 eruption (Fig. 4c) have increasing Mg# from core (Mg# 75-76) to rim (Mg# 79-80). For the 18/3/2012 product (Fig. 4d), clinopyroxene exhibits euhedral shapes and homogeneous compositions (Mg# 79-80) comparable to those observed for the phenocryst rims from the 4/3/2012 eruption.

Plagioclase phenocrysts are frequently zoned, with compositions (Fig. 5a) ranging from labradorite (An_{52-55}) to bytownite (An_{71-85}) and anorthite (An_{86-95}). The textural and chemical characteristics of plagioclase can be grouped following the nomenclature proposed by

Giacomoni *et al.* (2014). On this basis, Mt. Etna plagioclase are observed to record up to five dissolution-regrowth events that can involve both core and rim. Indeed, after plagioclase nucleation, the crystal growth stage may produce a common oscillatory zoning (Oz). Alternatively, four main types of dissolution textures can be recognized: rounded clear cores (C), dusty rounded (D_1), sieve textured (S), and patchy (P). After a regrowth (O_1) characterized by oscillatory zoning, plagioclase may exhibit two types of dissolution/regrowth texture at the rim, classified as (D_2) when made of dusty textures or (Mi) in the case of alignment of melt inclusions. Usually, a final overgrowth occurs before phenocryst is erupted (O_2).

Phenocrysts from the 8/9/2011 eruption (Fig. 5b) are characterized by rounded An-rich cores (An_{86-88}) without dusty textures (C), mantled by a more Ab-rich oscillatory zoned overgrowth (O_2, An_{64-72}). Phenocrysts from the 4/3/2012 eruption (Fig. 5c) have euhedral oscillatory zoned cores (Oz, An_{76-77}) and dusty rims (D_2, An_{63-78}), surrounded by more albitic overgrowths (O_2, An_{57-63}). Phenocrysts from the 18/3/2012 eruption (Fig. 5d) exhibit sub-rounded and dusty resorbed An-rich cores (D_1, An_{84-86}), resembling the dusty portions of 4/3/2012 plagioclases. The An-rich cores are surrounded by more albitic oscillatory zoned overgrowths (O_2 with An_{57-66}).

Opaque oxides are titanomagnetites ($Usp_{19.8-56.4}$). They occur either as phenocrysts (size ≤1 mm) in glomerophyric assemblages with clinopyroxene and olivine, or dispersed in the groundmass as single crystals (size <200 μm).

The matrix glass (Supplementary Online Material) is significantly enriched in silica and alkali with respect to the whole-rock analyses (see below), varying from basaltic trachyandesite (50.38 wt.% SiO_2, 7.64 Na_2O+K_2O wt.%) to tephriphonolite (49.48 wt.% SiO_2, 11.64 wt.% Na_2O+K_2O) with most analysis plotting in the field of phonotephrite (48.51-52.57 wt.% SiO_2, 8.34-10.50 wt.% Na_2O+K_2O).

DISCUSSION

Temporal changes of lava compositions and fractionation modelling

In Fig. 6, temporal compositional variations of erupted products have been evaluated in terms of changes in Mg# and CaO/Al_2O_3 ratio, showing that the 10/4/11 (Mg# 50.9) and 4/3/12 (Mg# 51.5) eruptions can be considered the most primitive in composition. From 18/2/2011 to 30/7/2011 events, at an almost constant Mg# of ~50.5, the CaO/Al_2O_3 ratio decreases from 0.63 to 0.57. For the 20/8/2011 eruption, the Mg# decreases significantly to 48.6, but the CaO/Al_2O_3 ratio does not changes substantially. After more or less pronounced chemical variations, both Mg# and CaO/Al_2O_3 ratio of the 4/3/2012 eruption increase to their maximum values of 51.5 and 0.68, respectively. This variation terminates with the 18/3/2012 and 24/4/2012 events, where Mg# and CaO/Al_2O_3 abruptly decrease to 48.3 and 0.60, respectively.

In order to verify the parental affinity of the erupted lavas and to quantify the extent of fractional crystallization, major- and trace-element mass-balance calculations have been performed for two distinct time-segments, i.e., from 18/2/2011 to 8/9/2011 (Step 1) and from 4/3/2012 to 24/4/2012 (Step 2). These time-segments were selected on the basis of their Mg# and CaO/Al_2O_3 variations, which suggest that a major recharge event reasonably occurred on 4/3/2012. The calculations were carried out by subtracting variable proportions of the solid assemblage whose mineral compositions are constrained by microprobe analyses of crystal cores. In particular, the subtracted mineral phases are olivine (Fo_{77}), clinopyroxene (Mg# 76), plagioclase (An_{74}), and titanomagnetite ($USP_{40.9}$) from the 18/2/2011 sample for the first time-segment, and then olivine (Fo_{77}), clinopyroxene (Mg# 73), plagioclase (An_{85}), and titanomagnetite ($USP_{28.9}$) from the 4/3/2012 sample for the second time-segment.

Petrographic features support these choice, and textural relationships in fact suggest that olivine is the liquidus phase followed by clinopyroxene, whereas plagioclase and magnetite crystallized at a late stage of magmatic differentiation.

The recalculated magma compositions were compared with the original whole-rock analyses of 8/9/2011 (Step 1) and 24/4/2012 (Step 2) eruptions. Note that the residual of square root of the sum of errors (r^2) for each calculation yield low values (0.18-0.27), indicative of reliable estimates.

We have also modelled the geochemical behaviour of HFSE (i.e., Nb, Zr, Hf, Th, U, Ta), REE (i.e., La, Ce, Cs, Nd, Sm, Eu, Gd, Dy, Er, Yb and Lu), and LILE (i.e., Sr, Rb, Ba) through the Rayleigh fractionation law:

$$C_l = C_0 \cdot F^{D-1}$$

where C_0 and C_l are the concentrations of the trace element in the original magma and remaining melt at the end of the fractional crystallization process, respectively. F is the melt fraction resulted after the major-element mass-balance calculation and D is the bulk partition coefficient of the element for the *n*-fractionating mineral phases:

$$D = \sum_i^n x_i \cdot K_{D_i}$$

with x_i as the weight fraction of mineral phase *i* and K_{Di} as the partition coefficient of the element in mineral phase *i*. Partition coefficients have been chosen from both natural and experimental datasets (Schnetzler & Philpotts, 1970; Shimizu, 1980; Villemant *et al.,* 1981; Fujimaki, 1984; Lemarchand, 1987; McKenzie & O'Nions, 1991; Nielsen *et al.,* 1992; Sobolev *et al.,* 1996; D'Orazio *et al.* 1997; Zack & Braum, 1998; Bindeman *et al.,* 1998; Vannucci *et al.,* 1998; Foley *et al.,* 2000; Wood & Trigila, 2001; Aignetorres *et al.,* 2007; Mollo *et al.,* 2013), measured in basaltic and alkali-basaltic melt compositions and reported in (Table 4 and Table 5). The relative percentage of error for each element has been calculated as the normalized difference between the modelled and the observed compositions:

$$r(x) = \left(\frac{Xm\text{-}Xr}{Xr}\right) * 100$$

where *r(x)* is the relative error for the element *x*, Xm is the concentration of the element in the residual melt, and *Xr* is the concentration of the element *x* in the starting melt composition.

Results for major and trace elements for Step 1 (from 18/2/2011 to 8/9/2011) and Step 2 (from 4/3/2012 to 24/4/2012) are reported in Table 4 and Table 5 respectively. Results from Step1 indicate that the 8/9/2011 major-element composition (Fig. 7a) is reproduced by fractionating a solid assemblage (f=14.6%) made of olivine (5.3%), clinopyroxene (40.9%), plagioclase (39.5%), and Ti-magnetite (14.3%) from the 18/2/2011 analysis, with r^2=0.18. On the other hand, results from Step 2 indicate that the 24/4/2012 major oxide analysis (Fig. 7b) is reproduced by fractionating from the 4/3/2012 composition a solid assemblage (f=12.6%) made of olivine (11.0%), clinopyroxene (54.9%), plagioclase (21.5%), and Ti-magnetite (14.3%), with r^2=0.27.

The primordial mantle-normalized pattern of trace element (Fig. 8) confirms the goodness of Step 1 and Step 2 calculations, evidencing as the percentage of error is generally low (1-5%) with only a few exceptions (6-10%).

Crystal-melt equilibrium conditions

According to previous Etnean studies of Armienti *et al.* (2012) and Giacomoni *et al.* (2016), near-equilibrium crystallization conditions are generally attained only between phenocryst cores and their host liquids (i.e., whole-rock analyses). Rationally, these phenocryst cores formed at the early stage of crystal nucleation and growth, before the original magma remarkably shifted towards more evolved compositions. (cf. Putirka, 2008). In contrast, phenocryst mantles and rims inevitably equilibrated with more evolved melts whose compositions, however, are not necessarily recorded by the natural products due to syn-eruptive groundmass crystallization. In this framework, we have tested the equilibrium of

olivine, clinopyroxene, and plagioclase cores from this study with their sample whole-rock analyses. In case of disequilibrium chemical features, the crystal cores have been tested for equilibrium with more primitive/evolved melt compositions from previous eruptive events.

The equilibrium crystallization of olivine has been tested through the Fe–Mg exchange reaction that is known to have a small dependence on melt composition, T, P, and fO_2, with an almost constant value of $^{ol\text{-}liq}Kd_{Fe–Mg} = 0.30 \pm 0.03$ (Roeder & Emslie, 1970). The Fe^{2+}/Fe^{3+} ratio is assumed to be close to 0.15, as calculated from the equation of Kress & Carmichael (1991) by assuming an oxygen fugacity between NNO and NNO+1. Three distinct cases can be distinguished for the 2011-2012 eruptions: 1) olivines within the equilibrium range of $^{ol\text{-}liq}Kd_{Fe–Mg}$ appearing in equilibrium with their host magma, 2) olivines with higher $^{ol\text{-}liq}Kd_{Fe–Mg}$ than that of equilibrium, because appearing equilibrated with more evolved magma and 3) olivines with $^{ol\text{-}liq}Kd_{Fe–Mg}$ appearing in equilibrium with more primitive magma.

Olivines from the 30/7/2011, 29/8/2011, and 8/9/2011 eruptions belong to cases 1) and 2). The equilibrium condition is attained in a range of $Fo_{76\text{-}79}$ olivine and Mg# 49-50 of the host melt, respectively (Black dots in Fig. 9 b-d-e). Olivines from the 18/2/2011, 20/8/2011, 4/3/2012, 18/3/2012, and 24/4/2012 eruptions belong to cases 1), 2), and 3). The attainment of equilibrium between olivine and melt is observed at $Fo_{73\text{-}79}$ and Mg# 48-51 (Black dots in Fig. 9 a-c-f-g-h).

The more evolved olivine crystals ($Fo_{71\text{-}76}$) for 18/2/2011, 30/7/2011, 29/8/201, 4/3/2012, and 18/3/2012, as well as $Fo_{70\text{-}74}$ for 20/8/2011, 8/9/2011, and 24/4/2012 are in disequilibrium with their corresponding whole rock data (Mg# 48-55), and instead appear in equilibrium with trachyandesitic matrix glass composition with (Mg# 45) (Table 6).

The more primitive olivine crystals ($Fo_{79\text{-}81}$) in 18/2/2011, 29/8/201, 4/3/2012, and 18/3/2012, as well as $Fo_{78\text{-}82}$ in 20/8/2011, and 24/4/2012) are out of equilibrium with their corresponding host rock (Mg# 48-55), and instead indicate equilibrium with a magma of composition similar

to that erupted during the 2006 event with Mg# 53 (Table 6), one of the most primitive trachybasalts of the recent Etnean eruptive history (Giacomoni *et al.,* 2014).

Some rare olivine crystals from 18/2/11 eruptions with Fo_{88} (Fig. 9a) indicate equilibrium with a melt composition resulting from the addition of 15% of a solid assemblage made of 64% olivine and 35% clinopyroxene from the 2006 eruptive event (Equilibrated 2006 in Table 6). The calculation procedure, as described in Giacomoni et al. (2014), consisted of the addiction of small proportions of olivine and clinopyroxene until the final melt composition (Mg# 68) yields a $^{Ol\text{-}melt}Kd_{Fe\text{-}Mg}$= 0.3 (Roeder & Emslie, 1970), corresponding to a fertile lherzolitic mantle assemblage.

Conversely, equilibrium of clinopyroxene has been tested assuming $^{cpx\text{-}melt}Kd_{Fe\text{-}Mg}$ = 0.27 ± 0.03, as indicated by Putirka *et al.* (2003). Most clinopyroxenes from 18/2/2011 (Fig. 10 a), 10/4/2011 (Fig. 10 b), 30/7/2011 (Fig. 10 c), 29/8/2011 (Fig. 10 e), 8/9/2011 (Fig. 10 f), and 18/3/2012 (Fig. 10 h) events plot within and above the equilibrium range that is derived for crystal compositions of Mg# 76-79. In contrast, clinopyroxenes from 20/8/2011 (Fig. 10 d) and 4/3/2012 (Fig. 10 g) eruptions have compositions (Mg# 80-83) below the equilibrium condition.

More differentiated clinopyroxenes above the equilibrium range result from equilibrium with the matrix glass (Mg# 45), whereas more primitive clinopyroxenes result from equilibrium the trachybasaltic magma composition (Mg# 53) of the 2006 event, as described in Giacomoni *et al.* (2014).

Plagioclase has been tested for equilibrium through the Ab-An exchange reaction, yielding $^{plg\text{-}melt}Kd_{Ab\text{-}An}$ = 0.27±0.11 at T ≥ 1050 °C (Fig. 11 a-h), as suggested by Putirka *et al.* (2008). Two distinct populations are observed: plagioclases with $An_{60\text{-}74}$ compositions are commonly in equilibrium with the whole-rock analyses of host magmas (CaO/Na_2O = 2.18-2.64; Mg# 48-55), whereas more anorthitic plagioclase ($An_{75\text{-}89}$) is out of equilibrium with their host

magmas, but in equilibrium with the whole-rock analysis of the 2006 eruption (CaO/Na_2O = 3.08; Mg# 53).

Intensive variables of magmatic crystallization (P-T-fO_2) and H_2O content

The crystallization temperature of olivine has been estimated using the geothermometer of Putirka *et al.* (2007), yelding an error of ± 25 °C (Fig. 12). The onset of crystallization is estimated at 1270 ± 27 °C, determined for Fo_{88} crystals in equilibrium with the reconstructed fertile lherzolitic mantle (Mg# 88; Giacomoni *et al.,* 2014). The olivine population (Fo_{78-84}) in equilibrium with the 2006 trachybasaltic magma (Mg# 53) formed at 1151-1178 °C. Phenocrysts (Fo_{74-79}) in equilibrium with host-rock compositions (Mg# 48-51) record crystallization temperatures of 1118-1139 °C. Finally, olivines (Fo_{70-75}) in equilibrium with matrix-glass compositions (Mg# 45) yield crystallization temperatures of 1121-1136 °C.

On the basis of equilibrium olivine and melt compositions, coupled with the estimated crystallization temperatures, four distinct groups are recognized: 1) Mm is exclusively represented by Fo_{88} crystals formed at 1270 °C and in equilibrium with a mantle-derived composition, 2) M0 includes Fo_{78-84} olivine in equilibrium with magma derived from the 2006 Etnean magma at 1151-1178 °C; 3) M1 includes Fo_{74-79} phenocrysts in equilibrium with the host rock compositions and crystallized at 1118-1139 °C; and 4) M2 includes the more evolved Fo_{70-75} olivines in equilibrium with residual-melt compositions (Mg# 45) at 1121-1136 °C. This classification presents several similarities with those presented by Kahl *et al.* (2011) except for the absence of Fo_{88} phenocrysts in equilibrium with calculated primary 2006 magma (Mg# 68).

Crystallization temperatures and pressures of clinopyroxene have been determined by means of the mineral-melt exchange reactions of diopside/hedembergite-jadeite and hedembergite/Ca-Tschermak as reappraised by Putirka (2008). The temperature has been estimated through the geothermometer of Putirka *et al.* (1996) which has the advantage of

being both pressure- and water-independent with an error ±25 °C. The derived temperature has been used as input data for the calculation of pressure with the H_2O-independent barometer of Putirka *et al.* (2003) with an error ±170 MPa. Results for each eruptive event are plotted in Fig. 13 a-h together with the saturation curve of clinopyroxene at 1 and 3 wt.% H_2O, as calculated by pMELTS (Ghiorso & Sack, 1995), using a starting composition equal to the whole-rock analysis of 4/3/2012 eruption and assuming the common Etnean oxygen fugacity of NNO+0.5 (Mollo *et al.,* 2015). Clinopyroxene saturates at 98-636 MPa and 1108-1158 °C, which falls in the thermal range comparable to M0, M1, and M3 olivine populations when the intrinsic error of each different thermometer is considered (Fig. 13). Clinopyroxene develops along two distinct crystallization paths corresponding to 2.5-2.8 wt.% H_2O and 3.0-3.2 wt.% and in a P-T range of 98-430 MPa and 120-636 MPa respectively.

Plagioclase crystallization temperature and dissolved H_2O content in the melt has been estimated by the plagioclase-melt thermometer of Putirka et al. (2003) and the plagioclase-melt hygrometer of Lange et al. (2011). Plagioclase stability is highly sensitivity to dissolved H_2O and T, and thus temperature estimation has been performed at a fixed pressure of 250 MPa, which is a reasonable value for anorthitic plagioclase nucleation from both pMELTS simulation (Giacomoni *et al.,* 2014, Mollo *et al.,* 2015) and experimental petrology (Metrich & Rutherford, 1998; Mollo *et al.* 2011). Calculation results show that plagioclase nucleates in a range of T from 1120 °C to 1050 °C in a magma with a melt with a dissolved H_2O content of 2.5 wt.% to 1.3 wt.% H_2O.

The 2011-2012 magmatic feeding system

Whole-rock geochemistry of the erupted products show significant variations through time. Eruptive events from 18/2/2011 to 20/8/2011 were fed by magma that become progressively more evolved. Fractionation modelling (Step 1) indicates that a crystallization assemblage of olivine, clinopyroxene, plagioclase, and Ti-magnetite was separated from the original 18/2/11 magma to form the 08/09/11 eruption. Magma erupted during the 4/3/12 event is more primitive geochemically (Mg# 51.5; CaO/Al_2O_3 = 3.13), indicating that an injection of less differentiated magma occurred before this eruptive event. Fractionation modelling (Step 2) indicates that the 24/4/12 magma can be formed by further crystallization of olivine, clinopyroxene, plagioclase, and Ti-magnetite (f=12.6 %) from the parental 4/3/12 magma.

The recharge event of 4/3/12 is recorded by changes in clinopyroxene and plagioclase chemical zoning (Fig. 4 and Fig. 5). Specifically, clinopyroxenes from the 4/3/12 eruption record an increase in Mg# from core (Mg# 75-76) to the rim (Mg# 79-80). In contrast, phenocrysts from the 18/3/12 eruption have higher Mg# values of an almost constant 79-81. Plagioclase compositions from the 4/3/12 lava reveal the input of more primitive, hotter (and possibly volatile-rich) magma, as indicated by the increase of An content from 55-63 to 78 in the dusty reaction zone. These observations are consistent with the experimental study of Tsuchiyama (1995) who reproduced dusty textures in albitic plagioclase by reacting crystals with more calcic and hotter melt. That study also demonstrated that, above the liquidus temperature, pre-existing phenocrysts react with the Ca-rich melt and recrystallize to a more anorthitic composition.

Results from crystal-melt equilibrium and thermobarometric estimations allow us to constrain the intensive conditions of crystallization and to subdivided the magmatic system into different crystallization environments by introducing the term of “magmatic facies”. A magmatic facies is a region in the feeding system, and not necessarily a specific magma batch or magma chamber, where crystallization is constrained by recurrent physical and chemical

conditions. In the case of Mt. Etna volcano, four distinct magmatic facies (i.e., F1, F2, F3, and F4) can be recognized.

The expression of F1 is only olivines from 18/2/11 lava with a composition of Fo_{88} (Mm) which crystallized at 1270 °C from a primary magma with an Mg# 68. The depth of crystallization can be estimated by extrapolating the clinopyroxene ΔP/ΔT path, calculated by regression of the entire clinopyroxene dataset. The estimated ΔP/ΔT path is almost constant at 9.4 MPa/ °C, with small variations (±0.4 MPa/ °C), considering the intrinsic error of the thermometer (±27 °C) and barometer (±170 MPa). Extrapolating the clinopyroxene ΔP/ΔT to 1270 °C suggests that the Fo_{88} olivine nucleated at ~1600 MPa, which is the equivalent to ~53 km b.s.l. This seems reasonable, considering previous thermobarometric data from Armienti *et al.* (2007) and pMELTS simulations, which indicate olivine liquidus between 1230-1290 °C for primary melts with 1-3 wt.% H_2O (Giacomoni *et al.* 2014).

F2 facies is recorded by olivine with Fo_{78-84} (M0) in equilibrium with the 2006 primitive composition and formed at 600-800 MPa and 1151-1178 °C. This facies corresponds to a depth range of 18-26 km b.s.l., in agreement with the mantle-lower crust transition zone identified by geophysical data (Finetti, 2005). According to mass balance calculations reported in Giacomoni *et al.* (2014), magma moving from F1 to F2 fractionates about 15% of a solid assemblage made of olivine (64%) and clinopyroxene (35%).

F3 facies is preserved by M1 (Fo_{74-79}) and M2 (Fo_{75-70}) olivine populations that are in equilibrium with the host rock (Mg# 48-55) and the matrix glass (Mg# 45) respectively. Considering the thermometer error of ± 25 °C, these two facies formed in a comparable thermal range of 1118-1139 °C and pressure of 250-450 MPa. Most clinopyroxene phenocrysts from this study preserve similar P-T conditions, suggesting it crystallized cotectically with olivine at H_2O contents of 2.5-3.3 wt.%, as derived by pMELTS computations (Fig. 13).

Finally, F4 facies is dominated by plagioclase crystallization at T ≤ 1120° in a magma with significantly reduced dissolved H_2O contents. According to the solubility model of Papale *et al.* (1999) for a magmatic mixture made of 3.5 wt.% H_2O and 0.4 wt.% CO_2 (Metrich *et al.,* 2004), H_2O exsolution would become significant at ~290 MPa.

Several studies have suggested that the feeding system of Mt. Etna lacks of a persistent and large magma chamber (Armienti *et al.,* 2012; Kahl *et al.,* 2011; Corsaro *et al.,* 2013 Giacomoni *et al.,* 2014; Mollo *et al.,* 2015), and instead is characterized by polybaric fractionation through a vertically-developed open-conduit and, occasionally, in small magma batches even located within the volcanic edifice (Tanguy et al., 1997; Viccaro *et al.,* 2005; Ferlito *et al.,* 2009; Giacomoni *et al.,* 2012; Corsaro *et al.,* 2013). Under such circumstances, the petrographical and geochemical characteristics of erupted magmas would be governed by: i) the initial volatile content of the magma (Metrich & Rutherford, 1998), ii) the residence time in a specific magmatic facies, and iii) the degree of undercooling, which is controlled mainly by the H_2O-exsolution during ascent towards the surface (Mollo *et al.* 2013).

The coexistence of phenocrysts equilibrated in different magmatic facies in products from temporally close-related eruptive events indicates a dynamic continuous magmatic system, characterized by a vertical zoning in pressure, temperature, and H_2O content gradients leading to crystallization of phenocrysts equilibrated at different conditions.

As a whole, the physicochemical evolution of the magmatic system feeding the 2011-2012 paroxysmal eruptions at Mt. Etna volcano is schematized in Fig. 14. Mt. Etna central conduits are persistently filled with a magmatic column, fluctuating due to internal pressure and changes in buoyancy (Corsaro *et al.,* 2004) but, we should consider a hypothetical stage in which the entire feeding system is filled with basic magma (Mg# 53) with up to 3.7 wt.% of dissolved H_2O (Fig. 14 a). The composition of this basic magma is comparable with those emitted during the 2006 event or preserved in olivine-hosted melt inclusions. (Metrich &

Rutherford, 1998; Kamenetsky *et al.,* 2007). Despite its basic geochemical features, mass balance and MELTS simulations (Giacomoni *et al.,* 2014) demonstrate that the 2006 magma cannot be considered as a primary melt, but instead underwent 15% fractionation from the mantle source.

Once in the crustal feeding system, gradients in temperature, pressure and volatile content (mainly H_2O), lead to a vertical differentiation and zoning that results in various magmatic facies (Fig. 14 b). Starting from the top, the shallower portion of the feeding system is characterized by massive volatile exsolution that leads to plagioclase crystallization and fractionation.

At pressures ranging between 450 MPa and 250 MPa and temperatures from 1139 °C to 1118 °C, magmatic crystallization is mainly limited to olivine (Fo_{74-79}) and clinopyroxene in F3. Geophysical tomographic studies (De Gori *et al.,* 2005; Patané *et al.,* 2006) recognize a high velocity layer interpreted as an intrusive body that could be reasonably made of a crystal mush fractionated in the F3 facies.

The F2 facies is located at the MOHO depth, from 600 MPa to 800 MPa at magmatic temperature ranging from 1178 °C to 1151 °C. Finally, F1 facies represents the deepest portion of the feeding system, but is only preserved by rare Fo_{88} olivine crystals, formed at 1270 °C at 1600 MPa (Giacomoni *et al.,* 2014). In this vertically zoned feeding system, magmas erupted during each event carries phenocrysts equilibrated in the various magmatic facies.

CONCLUDING REMARKS

On the basis of textural, chemical, and petrological analyses of minerals and whole rock data, the 2011-2012 eruptive activity at Mt. Etna volcano can be interpreted as follows:

- The central conduits of Mt. Etna that fed the 2011-2012 eruptive events were characterized by a continuous vertically zoned feeding system;
- Four main magmatic facies have been recognized: F1, 1600 MPa at 1270 °C (Ol Fo_{88}); F2, 800 MPa to 600 MPa at 1178 °C to 1151 °C (Ol Fo_{84-78}); F3, 450 MPa to 250 MPa at 1139 °C to 1118 °C (Ol Fo_{79-74}); F4, <250 MPa at <1120 °C (Ol Fo_{75-70});
- Magmas erupted on 30/7/11, 29/8/11, 8/9/11, 18/3/11 and 24/4/12 were mostly fed from F3 and F4 facies;
- Magmas from the F2 facies were intruded in the shallower portion of the feeding system during the 18/2/11, 20/8/11, and a main mafic recharge occurred during the 4/3/12 event;
- The deepest facies F1, sited at mantle pressure, is preserved only as Fo_{88} olivine and rarely reach the surface. Melts in equilibrium (Mg# 68) have been found in melt inclusions and modelled by mass-balance fractionation from basic 2006 trachybasaltic composition.

ACKNOWLEDGMENTS

We are really gratefully to M. Masotta and C. Pallares as reviewers for their useful and constructive criticism. Authors thanks also J. Gardner for his precious editorial guidance. Finally, a thanks to M. Nazzari (INGV-Section of Roma) and R. Tassinari (UNIFE) for their valuable contribution during analytical sessions.

REFERENCES

Aignertorres, M., Blundy, J., Ulmer, P. and Pettke, T. (2007). Laser Ablation ICP-MS study of trace element partitioning between plagioclase and basaltic melts: an experimental approach. *Contribution to Mineralogy and Petrology* **153**, 647-667.

Aiuppa, A., Cannata, A., Cannavò, F., Di Grazia, G., Ferrari, F., Giudice, G., Gurrieri, S., Liuzzo, M., Mattia, M., Montalto, P., Patanè, D., Puglisi, G. (2010). Patterns in the recent 2007–2008 activity of Mount Etna volcano investigated by integrated geophysical and geochemical observations. *Geochemistry Geophysics Geosystems* **11**, Q09008. http://dx.doi.org/10.1029/2010GC003168.

Aloisi, M., Bonaccorso, A., Cannavò, F., Gambino, S., Mattia, M., Puglisi, G., Boschi, E. (2009). A new dike intrusion style for the Mount Etna May 2008 eruption modelled through continuous tilt and GPS data, *Terra Nova* **21**, 316-321.

Andronico, D., Branca, S., Calvari, S., Burton, M., Caltabiano, T., Corsaro, R.A., Del Carlo, P., Garfì, G., Lodato, L., Miraglia, L., Murè, F., Neri, M., Pecora, E., Pompilio, M., Salerno, G., Spampinato, L. (2005). A multidisciplinary study of the 2002-03 Etna eruption. Insights into a complex plumbing system. *Bulletin Of Volcanology* **67**: 314-330.

Andronico, D., Scollo, S., Cristaldi, A., Caruso, S. (2008). The 2002–2003 Etna explosive activity: tephra dispersal and features of the deposit. *Journal of Geophysical Research of Solid Earth* **113**, B04209. http://dx.doi.org/10.1029/2007JB005126.

Armienti, P., Tonarini, S., Innocenti, F., D'Orazio, M. (2007). Mount Etna pyroxene as tracer

of petrogenetic processes and dynamics of the feeding system. *Geological Society of America Special Paper*, **418**.

Armienti, P., Perinelli, C., Putirka, K. (2012). A new model to estimate deep-level magma ascent rates, with applications to Mt. Etna (Sicily, Italy). *Journal of Petrology*, 1-19, doi:10.1093/petrology/egs085.

Behncke, B., Branca, S., Corsaro, R.A., De Beni, E., Miraglia, L., Proietti, C., (2014). The 2011-2012 summit activity of Mount Etna: Birth, growth and products of the new SE crater. *Journal of Volcanology and Geothermal Research* **270**, 10-21.

Behncke, B., Neri, M. (2003). The July-August 2001 eruption of Mt. Etna (Sicily). *Bulletin of Volcanology* **65**, 461-476.

Bindeman, I.N., Davis, A.M. and Drake, M.J. (1998). Ion microprobe study of plagioclase-basalt partition experiments at natural concentration levels of trace elements. *Geochimica et Cosmochimica Acta* **62**, 1175-1193.

Bonaccorso, A., Bonforte, A., Currenti, G., Del Negro, C., Di Stefano, A., Greco, F. (2011). Magma storage, eruptive activity and flank instability: inferences from ground deformation and gravity changes during the 1993–2000 recharging of Mt. Etna volcano. *Journal of Volcanology and Geothermal Research* **200**, 245-254.

Bonaccorso, A., Calvari, S., Currenti, G., Del Negro, C., Ganci, G., Linde, A., Napoli, R., Sacks, S., Sicali, A. (2013). From source to surface: dynamics of Etna's lava fountains investi-gated by continuous strain, magnetic, ground and satellite thermal data. *Bulletin of Volcanology* **75**, 690.

Branca, S., Coltelli, M., De Beni, E., Wijbrans, J. (2008). Geological evolution of Mount Etna

volcano (Italy) from earliest products until the first central volcanism (between 500 and 100 ka ago) inferred from geochronological and stratigraphic data. *International Journal of Earth Sciences* **97**, 135-152.

Calvari, S., Salerno, G.G., Spampinato, L., Gouhier, M., La Spina, A., Pecora, E., Harris, A.J.L., Labazuy, P., Biale, E., Boschi, E. (2011). An unloading foam model to constrain Etna's 11-13 January 2011 lava fountaining episode. *Journal of Geophysical Research* **116**.

Corsaro, R.A., Civetta, L., Di Renzo, V., Miraglia, L. (2009). Petrology of lavas from the 2004–2005 flank eruption of Mt. Etna, Italy: inferences on the dynamics of magma in the shallow plumbing system. *Bulletin of Volcanology* **71**, 781-793.

Corsaro, R.A., Di Renzo, V., Di Stefano, S., Miraglia, L., Civetta, L. (2013). Relationship between petrologic processes in the plumbing system of Mt. Etna and the dynamics of the eastern flank from 1995 to 2005. *Journal of Volcanology and Geothermal Research* **251**, 75-89.

Corsaro, R.A., Pompilio, M. (2004). Buoyancy-controlled eruption of magmas at Mount Etna. *Terra Nova* **16**, 16-22.

D'Orazio, M., Tonarini, S., Innocenti, F. & Pompilio, M. (1997). Northern Valle del Bove volcanic succession (Mount Etna, Sicily): Petrography, geochemistry and Sr-Nd isotope data. *Acta Vulcanologica* **9**, 73-86.

De Beni, E., Behncke, B., Branca, S., Nicolosi, I., Carluccio, R., Caracciolo, D'Ajello, F., Chiappini, M. (2005). The continuing story of Etna's New Southeast Crater (2012–2014): evolution and volume calculations based on field surveys and aerophotogrammetry. *Journal of Volcanology and Geothermal Research* **303**: 175-186.

De Gori, P., Chiarabba, C., Patanè, D. (2005). Qp structure of Mt. Etna: constraints for the physics of the plumbing system. *Journal of Geophysical Research* **110**.

Di Grazia, G., Falsaperla, S., Langer, H. (2006). Volcanic tremor location during the 2004 Mount Etna lava effusion. *Geophysical Research Letters* **33**, L04304.

Ferlito, C., Coltorti, M., Cristofolini, R., Giacomoni, P.P., (2009). The contemporaneous emission of low-K and high-K trachybasalts and the role of the NE Rift during the 2002 eruptive event, Mt. Etna, Italy. *Bulletin of Volcanology* **71**, 575-587.

Ferlito, C., Viccaro, M., Nicotra, E., Cristofolini, R. (2010). Relationship between the flank sliding of the South East Crater (Mt. Etna, Italy) and the paroxysmal event of November 16, 2006. *Bulletin of Volcanology* **72**, 1179-1190.

Finetti, I.R. (2005). Depth contour map of the Moho discontinuity in the central Mediterranean region from new crop seismic data. In: *Finetti, I.R. (Ed.), CROP PROJECT. Deep Seismic Exploration of the Central Mediterranean and Italy*, 597-606.

Foley, S.F., Barth, M.G. and Jenner, G.A. (2000). Rutile/melt partition coefficients for trace elements and an assesments of the influence of rutile on the trace element characteristics of subduction zone magmas. *Geochimica et Cosmochimca Acta* **64**, 933-838.

Fujimaki, H., Tatsumoto, M. and Aoki, K.-i. (1984). Partition coefficients of Hf, Zr, and REE between phenocrysts and groundmass. *Journal of Geophysical Research* **89**, 662-672.

Ghiorso, M.S., Sack, R.O. (1995). Chemical mass transfer in magmatic processes IV. A revised and internally consistent thermodynamic model for the interpolation and extrapolation of liquid-solid equilibria in magmatic systems at elevated temperatures and pressures.

Contribution to Mineralogy and Petrology **119**, 197-212.

Giacomoni, P.P., Coltorti, M., Bryce, J.G., Fahnestock, M.F., Guitreau, M. (2016). Mt. Etna plumbing system revealed by combined textural, compositional, and thermobarometric studies in clinopyroxene. *Contribution to Mineralogy and Petrology* **171**:34.

Giacomoni, P.P., Ferlito, C., Alesci, G., Coltorti, M., Monaco, C., Viccaro, M., Cristofolini, R., (2012). A common feeding system of the NE and S rifts as revealed by the bilateral 2002/2003 eruptive event at Mt. Etna (Sicily, Italy). *Bulletin of Volcanology* **74**, 2415-2433.

Giacomoni, P.P., Ferlito, C., Coltorti, M., Bonadiman, C., Lanzafame, G. (2014). Plagioclase as archive of magma ascent dynamics on "open conduit" volcanoes: the 2001–2006 eruptive period at Mount Etna. *Earth Science Review* **138**, 371-393.

Gillot, P.Y., Keiffer, G., Romano, R. (1994). The evolution of Mount Etna in the light of potassium-argon dating. *Acta Vulcanologica* **5**, 81-87.

Iezzi, G., Mollo, S., Shaini, E., Cavallo, A., Scarlato, P. (2014). The cooling kinetics of plagioclase revealed by electron microprobe mapping, *American Mineralogy*, http://dx.doi.org/10.2138/am.2014.4626.

Irvine, T. N. (1965). Chromian spinel as a petrogenetic indicator. Part I. Theory. *Canadian Journal of Earth Sciences* **2**, 648-72.

Kahl, M., Chakraborty, S., Costa, F., Pompilio, M. (2011). Dynamic plumbing system beneath volcanoes by kinetic modeling, and the connection to monitoring data: an example from Mt. Etna. *Earth and Planetary Science Letters* **308**, 11-22.

Kahl, M., Chakraborty, S., Costa, F., Pompilio, M., Liuzzo, M., Viccaro, M. (2013). Compositionally zoned crystals and real-time degassing data reveal changes in magma

transfer dynamics during the 2006 summit eruptive episodes of Mt. Etna. *Bulletin of Volcanology* **75**, 692.

Kieffer, G. (1975). Pillows and hyaloclastites associated to subaerial lavas at the southwest of the base of Mount Etna (Sicily, Italy). *Geology of Mediteranean* **77,** 179-184.

Kress, V.C. and Carmichael, I.S.E. (1991). The compressibility of silicate liquids containing Fe_2O_3 and the effect of composition, temperature, oxygen fugacity and pressure on their redox states. *Contribution to Mineralogy and Petrology* **108**, 82-92.

Lachance, G.R., Traill, J.R. (1966). Practical solution to the matrix problem in X-ray analysis. *Canadian Spectroscopy* **11**. 43-48.

Le Maitre, R. (2002). Igneous rocks: a classification and glossary of terms. *Cambridge University Press*, Cambridge.

Lemarchand, F., Benoit, V. and Calais, G. (1987). Trace element distribution coefficients in alkaline series. *Geochimica et Cosmochimica Acta* **51**, 1071-1081.

Lundgren, P., Berardino, P., Coltelli, M., Fornaro, G., Lanari, R., Puglisi, G., Sansosti, E., Tesauro, M. (2003). Coupled magma chamber in action and sector collapse slip observed with synthetic aperture radar interferometry on Mt. Etna volcano. *Journal of Geophysical Research* **108**, 2247-2267.

McDonough, W.F., Sun, S.S. (1995). The composition of the Earth. *Chemical Geology*, **120,** 223-253.

McKenzie, D. and O'Nions, R.K. (1991). Partial melt distributions from inversion of rare Earth element concentrations. *Journal of Petrology* **32**, 1021-1091.

Métrich, N., Allard, P., Spilliert, N., Andronico, D., Burton, M. (2004). 2001 flank eruption of the alkali- and volatile-rich primitive basalt responsible for Mount Etna's evolution in the last three decades. *Earth and Planetary Science Letters* **228**, 1-17.

Métrich, N., Rutherford, M.J. (1998). Low pressure crystallization paths of H_2O-saturated basaltic-hawaiitic melts from Mt Etna: implications for open-system degassing of basaltic volcanoes. *Geochimica and Cosmochimica Acta* **62**, 1195-1205.

Mollo, S., Giacomoni, P.P., Andronico, D., Scarlato, P. (2015b). Clinopyroxene and titanomagnetite cation redistributions at Mt. Etna volcano (Sicily, Italy): footprints of the final solidification history of lava fountains and lava flows. *Chemical Geology* **406**, 45-54.

Mollo, S., Giacomoni, P.P., Coltorti, M., Ferlito, C., Iezzi, G., Scarlato, P. (2015a). Reconstruction of magmatic variables governing recent Etnean eruptions: constraints from mineral chemistry and P-T-fO_2-H_2O modelling. *Lithos* **212-215**, 311-320.

Mollo, S., Giacomoni, P.P., Coltorti, M., Ferlito, C., Iezzi, G., Scarlato, P. (2015a). Reconstruction of magmatic variables governing recent Etnean eruptions: constraints from mineral chemistry and P-T-$f0_2$-H_2O modelling. *Lithos* **212-215**, 311-320.

Mollo, S., Lanzafame, G., Masotta, M., Iezzi, G., Ferlito, C., Scarlato, P. (2011). Cooling history of a dyke as revealed by mineral chemistry: a case study from Mt. Etna volcano. *Chemical Geology* **288**, 39-52.

Mollo, S., Putirka, K., Misiti, V., Soligo, M., Scarlato, P. (2013). A new test for equilibrium based on clinopyroxene-melt pairs: clues on the solidification temperatures of Etnean alkaline melts at post-eruptive conditions. *Chemical Geology* **352**, 92-100.

Monaco, C., Catalano, S., Cocina, O., De Guidi, G., Ferlito, C., Gresta, S., Musumeci, C., Tortorici, L. (2005). Tectonic control on the eruptive dynamics at Mt. Etna Volcano (Sicily) during the 2001 and 2002–2003 eruptions. *Journal Of Volcanology and Geothermal Research* **144**, 211-233.

Morimoto, N. (1988). Nomenclature of pyroxenes. *Mineralogical Magazine*, **52**, 535-550.

Neri, M. (2010). Rapporto settimanale sull'attività eruttiva dell'Etna (10–16 Maggio). Report INGV of May 10-16, 2010 from www.ct.ingv.it (in Italian).

Nielsen, R.L., Gallahan, W.E. and Newberger, F. (1992). Experimentally determined mineral-melt partition coefficients for Sc, Y and REE for olivine, orthopyroxene, pigeonite, magnetite and ilmenite. *Contribution to Mineralogy and Petrology* **110**, 488-499.

Papale, P. (1999). Modeling of the solubility of a two-component H_2O+CO_2 fluid in silicate liquids. *American Mineralogist* **84**, 477-492.

Patanè, D., Aiuppa, A., Aloisi, M., Behncke, B., Cannata, A., Coltelli, M., Di Grazia, G., Gambino, S., Gurrieri, S., Mattia, M., Salerno, G. (2013). Insights into magma and fluid transfer at Mount Etna by a multi-parametric approach: a model of the events leading to the 2011 eruptive cycle. *Journal of Geophysical Research* **118**, 1-21.

Patanè, D., Barberi, G., Cocina, O., De Gori, P., Chiarabba, C. (2006). Time-resolved seismic tomography detects magma intrusions at Mount Etna. *Science* **313**, 821-825.

Patanè, D., G. Barberi, O. Cocina, P. De Gori, and C. Chiarabba (2006). Time-resolved seismic tomography detects magma intrusions at Mount Etna, *Science* **313**, 821-823.

Peccerillo, A. (2005). Plio-quaternary Volcanism in Italy - Petrology, Geochemistry,

Geodynamics. Springer-Verlag, Berlin, 365.

Putirka, K. D. (2008). Thermometers and barometers for volcanic systems. In: Putirka, K. D. & Tepley, F. J., III (eds) Minerals, Inclusions and Volcanic Processes. Mineralogical Society of America and Geochemical Society, *Reviews in Mineralogy and Geochemistry* **69**, 61-120.

Putirka, K., Johnson, M., Kinzler, R., Walker, D. (1996). Thermobarometry of mafic igneous rocks based on clinopyroxene-liquid equilibria, 0-30 Kbar. *Contribution to Mineralogy and Petrology* **123**, 92-108

Putirka, K., Perfit, M., Ryerson, F.J., Jackson M.G. (2007). Ambient and excess mantle temperatures, olivine thermometry, and active vs. passive upwelling. *Chemical Geology* **241**, 177-206.

Putirka, K., Ryerson, F.J., Mikaelian, H. (2003). New igneous thermo- barometers for ma c and evolved lava compositions, based on clinopyroxene + liquid equilibria. *American Mineralogist* **88**, 1542-1554.

Roeder, P. L. and Emslie, R. F. (1970). Olivine-liquid equilibrium. *Contributions to Mineralogy and Petrology* **29**, 275-289.

Schiavi, F., Rosciglione, A., Kitagawa, H., Kobayashi, K., Nakamura, E., Mario Nuccio, P., Ottolini, L., Paonita, A., Vannucci, R., (2015). Geochemical heterogeneities in magma beneath Mount Etna recorded by 2001-2006 melt inclusions. *Geochemistry Geophysics Geosystems*, d.o.i. 10.1002/2015GC005786.

Schnetzler, C.C. and Philpotts, J.A. (1970). Partition coefficients of rare-earth elements between igneous matrix material and rock-forming mineral phenocrysts. *Geochimica et Cosmochimica Acta* **34**, 331-340.

Sharp, A.D.L, Davis, P.M., Gray, F. (1980). A low velocity zone beneath Mount Etna and magma storage. *Nature* **287**, 587-591.

Shimizu, H. (1980). Experimental study on rare-earth element partitioning in minerals formed at 20 and 30 Kbar for basaltic systems. *Geochemical Journal* **14***,* 185-202.

Sobolev, A.V., Migdisov, A.A. and Portnyagin, M.V. (1996). Incompatible element partitioning between clinopyroxene and basalt liquid revealed by the study of melt inclusions in minerals from Troodos lavas, Cyprus. *Petrology* **4**, 307-317.

Tanguy, J.C., Condomines, M., Kieffer, G. (1997). Evolution of Mount Etna magma: constraint on the present feeding system and eruptive mechanism. *Journal of Volcanology and Geothermal Research* **75**, 221-250.

Tsuchiyama, A. (1985). Dissolution kinetics of plagioclase in the melt of the system diopside–albite–anorthite, and the origin of dusty plagioclase in andesites. *Contribution to Mineralagy and Petrology* **89**, 1-16.

Vannucci, R., Bottazzi, P., Wulffpedersen, E. and Neumann, E. (1998). Partitioning of REE, Y, Sr, Zr and Ti between clinopyroxene and silicate melts in the mantle under La Palma (Canary Islands): implications for the nature of the metasomatic agents. *Earth and Planetary Science Letters* **158**, 39-51.

Viccaro, M., Ferlito, C., Cortesogno, L., Cristofolini, R., Gaggero, L. (2005). Magma mixing during the 2001 event at Mount Etna (Italy). Effects on the eruptive dynamics. *Journal of Volcanology and Geothermal Research* **149**, 139-159.

Viccaro, M., Calcagno, R., Garozzo, I., Giuffrida, M., Nicotra, E. (2015). Continuous magma

recharge at Mt. Etna during the 2011-2013 period controls the style of volcanic activity and compositions of erupted lavas. *Mineralogy and Petrology* **109**, 67-83.

Viccaro, M., Giacomoni, P.P., Ferlito, C., Cristofolini, R. (2010). Dynamics of magma supply at Mt. Etna volcano (Southern Italy) as revealed by textural and compositional features of plagioclase phenocrysts. *Lithos* **116**, 77-91.

Villemant, B., Jaffrezic, H., Joron, J.L. and Treuil, M. (1981). Distribution coefficients of major and trace-elements – fractional crystallization in the alkali basalt series of Chainde-Des-Puys (Massif Central, France. *Geochimica et Cosmochimica Acta* **45**, 1997-2016.

Wood, B. and Trigila, R. (2001). Experimental determination of aluminour clinopyroxene-melt partition coefficients for potassic liquids, with application to the evolution of the Roman province potassic magmas. *Chemical Geology* **172,** 213-223.

Zack, T. and Brumm, R. (1998). Ilmenite/liquid partition coefficients of 26 trace elements determined through ilmenite/clinopyroxene partitioning I garnet pyroxene. In: 7th International Kimberlite Conference. Gurney, J.J., Gurney, J.L., Pascoe, M.D. and Richardson, S.H. (Editors), Red Roof Design, Cape Town. 986-988.

FIGURE CAPTIONS

Figure 1

Regional geological map of Sicily showing position of Mt. Etna and main structural features (a). Maps of lava field and emission vents of the studied 2011-2012 eruptive events; b) 18/2/2011, c) 10/4/2011, d) 12/5/2011, e) 30/7/2011, f) 20/8/2011, g) 29/8/2011, h) 8/9/2011, i) 4/3/2012, j) 18/3/2012 and k) 24/4/2012.

Figure 2

Whole-rock geochemistry of studied products. a) Total Alkalis vs Silica (wt.%) diagram (Le Maitre, 2002). b) Harker variation diagram, MgO (wt.%) vs TiO_2 (wt.%), CaO (wt.%), Na_2O (wt.%), and K_2O (wt.%).

Figure 3

Primordial mantle-normalized whole-rock trace-element diagram (McDonough & Sun, 1995). Basic magma composition of 4/3/12 eruptive event is shown in red line.

Figure 4

Classification and compositional core-rim zoning of clinopyroxene. a) Classification diagram of clinopyroxene (Morimoto, 1988); b) Core-rim Mg# compositional profile of clinopyroxene erupted during the 8/9/11 event; c) Core-rim Mg# compositional profile of clinopyroxene erupted during the 4/3/12 event; d) Core-rim Mg# compositional profile of clinopyroxene erupted during the 18/3/12 event.

Figure 5

Classification and compositional core-rim zoning of plagioclase. a) Classification diagram of studied plagioclase; b) Core-rim anorthite compositional profile of plagioclase erupted during the 8/9/11 event; c) Core-rim anorthite compositional profile of plagioclase erupted during the 4/3/12 event; d) Core-rim anorthite compositional profile of plagioclase erupted during the 18/3/12 event.

Figure 6

Temporal changes in compositional whole-rock compositions of Mg# (a) and CaO/Al_2O_3 (b) of 2011-2012 eruptive events.

Figure 7

SiO_2 vs (a) CaO/Al_2O_3 and (b) Na_2O+K_2O resulting from mass-balance fractionation modelling. Fractionation vectors are shown for Step 1, from 18/2/11 to 8/9/11 and Step 2, from 4/3/12 to 24/4/2012. Results are reported as wt.% of relative mineral abundance and percentage of fractionated solid (f).

Figure 8

Spider diagrams of trace elements abundances normalized to primordial mantle showing results from mass-balance fractionation modelling for (a) Step 1 and (b) Step 2. Black patterns are starting magma compositions, grey patterns are residual compositions. The modelled composition is represented in red, with the relative error (%) for each element.

Figure 9

Olivine crystal-melt equilibrium conditions as $^{Ol\text{-}melt.}Kd_{Mg\text{-}Fe}$ versus forsterite (Fo) content of phenocryst from 18/2/2011 (a), 30/7/2011 (b), 20/8/2011 (c), 29/8/2011 (d), 8/9/2011 (e), 4/3/2012 (f), 18/3/2012 (g) and 24/4/2012 (h). Calculated $^{Ol\text{-}melt.}Kd_{Mg\text{-}Fe}$ after re-equilibration are shown as blue (host rock Mg# 45), red dots (host rock Mg# 53) and white dots (host rock Mg# 68).

Figure 10

Clinopyroxene crystal-melt equilibrium conditions as $^{Cpx\text{-}melt.}Kd_{Mg\text{-}Fe}$ versus Mg# of phenocryst from 18/2/2011 (a), 10/4/2011 (b), 30/7/2011 (c), 20/8/2011 (d), 29/8/2011 (e), 8/9/2011 (f), 4/3/2012 (g), 18/3/2012 (h). Calculated $^{Cpx\text{-}melt.}Kd_{Mg\text{-}Fe}$ after re-equilibration are shown as blue (host rock Mg# 45) and red dots (host rock Mg# 53).

Figure 11

Plagioclase crystal-melt equilibrium conditions as $^{Plg\text{-}meld.}Kd_{Ab\text{-}An}$ versus anorthite (An%) of phenocryst from 18/2/2011 (a), 10/4/2011 (b), 30/7/2011 (c), 20/8/2011 (d), 29/8/2011 (e), 8/9/2011 (f), 4/3/2012 (g), 18/3/2012 (h). Calculated $^{Plg\text{-}meld.}Kd_{Ab\text{-}An}$ after re-equilibration are shown as blue (host rock Ca/Na = 2.09) and red dots (host rock Ca/Na = 3.7).

Figure 12

Results from olivine-melt thermometer of Putirka *et al.* (2007) plotted in a Fo in olivine vs temperature diagram. Coloured dots are shown together with their $^{Ol\text{-}melt.}Kd_{Mg\text{-}Fe}$ equilibrium range. Blue dots equilibrated with host rock Mg# 45, black dots equilibrated with sample

whole rock composition (Mg# 48-51) red dots equilibrated with 2006 basic trachybasaltic composition (Mg# 53) and white dots equilibrated with mantle equilibrated 2006 composition (Mg# 68).

Figure 13

Results from clinopyroxene-melt thermometer (Putirka *et al.,* 1996) and barometer (Putirka *et al.,* 2003). Dashed lines are pMELTS (Ghiorso & Sack, 1995) modelled clinopyroxene liquidus line for 1 wt.%, 2 wt.% and 3wt.% dissolved H_2O in the melt.

Figure 14

Schematic diagram of the central conduits of Mt. Etna that fed the 2011-2012 eruptive events. a) hypothetical initial phase with the whole conduit filled with compositional homogeneous magma (Mg# 53); b) The conduit become vertically zoned into four main magmatic facies. H_2O solubility curve has been calculated with the model of Papale *et al.* (1999) starting from 3.7 wt.% H_2O and 0.8 wt.% of CO_2. See text for details.

TABLE CAPTIONS

Table 1

Date and timing of the 2011-2012 eruptive events; emission date in bold are those sampled and studied in this study.

Table 2

Petrographic features of studied products: relative proportions of phenocrysts (%), porphyritic index (%), percentage of vesicles (%) and type of groundmass.

Table 3

Whole-rock major (wt.%) and trace element (ppm) analyses of studied samples emitted during the 2011/2012 eruptive events. REE, U, Th and Hf determined by ICP-MS, other elements by XRF. Loss on ignition (L.O.I) was determined by gravimetric methods assuming Fe_2O_3= 0.15 FeO. Mg#= Mg/(Mg+Fe) mol %.

Table 4

Major and trace element mass balance fractionation modelling results for Step 1: from 18/2/11 to 8/9/11. Crystal-melt partition coefficients were chosen from Villemant (1981); Shimizu (1980), Fujimaki *et al.* (1984); Lemarchand (1987) McKenzie & O'nions (1991); Zack & Braum (1998); Ewart & Griffin (1994); Vannucci et al. (1998); Bindeman et al. (1998); Foley et al. (2000); Aignertorres et al. (2007); Wood & Trigila (2001);

Table 5

Major and trace element mass balance fractionation modelling results for Step 2: from 4/3/12 to 24/4/12. Crystal-melt partition coefficients were chosen from Villemant (1981); Shimizu (1980), Fujimaki *et al.* (1984); Lemarchand (1987) McKenzie & O'nions (1991); Zack & Braum (1998); Ewart & Griffin (1994); Vannucci et al. (1998); Bindeman et al. (1998); Foley et al. (2000); Aignertorres et al. (2007); Wood & Trigila (2001);

Table 6

Major element composition of melts for test for crystal-melt equilibrium. Iron partitioning calculated assuming Fe_2O_3 = 0.15 FeO. Mg# = Mg/(Mg+Fe) mol %.

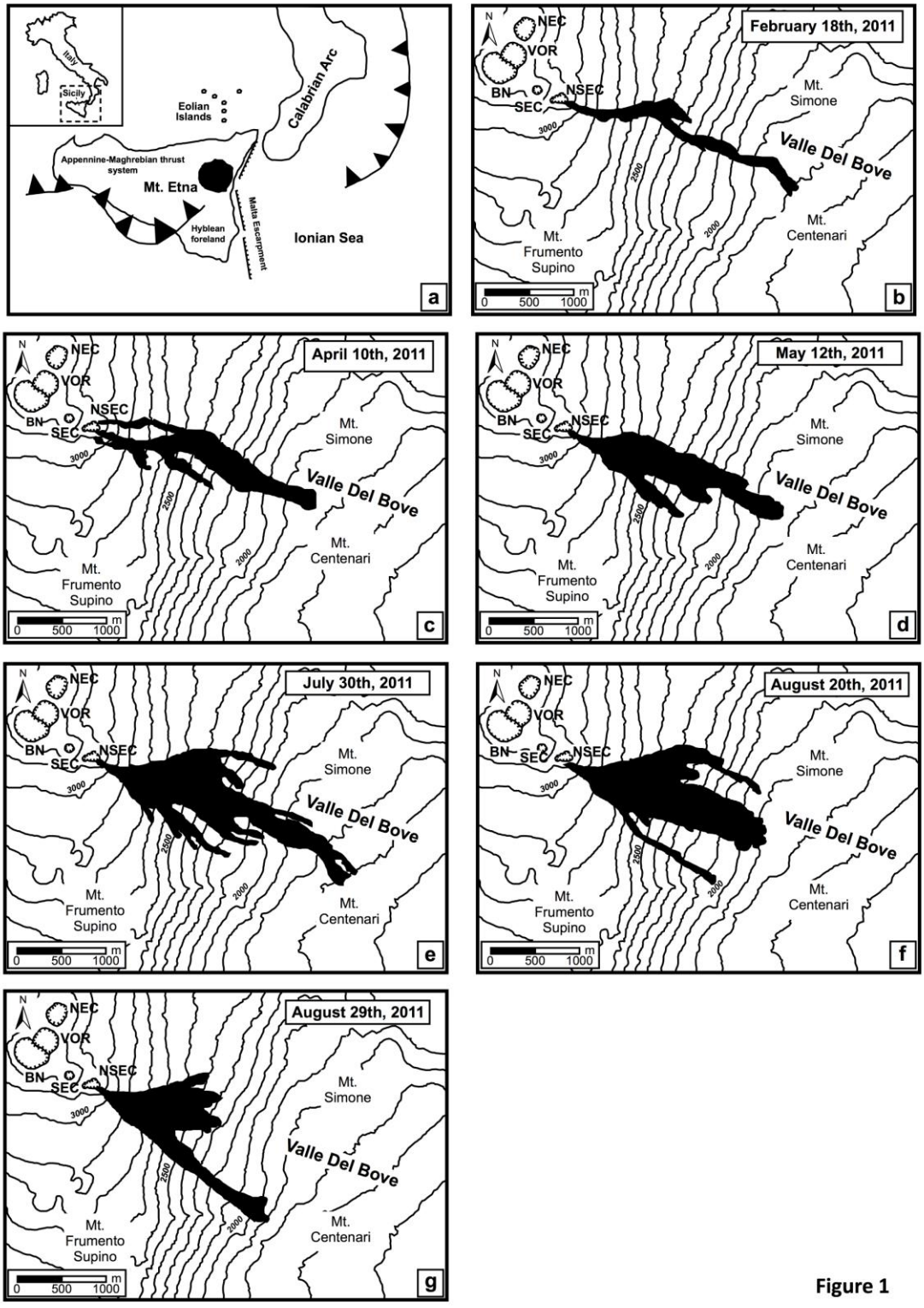

Figure 1

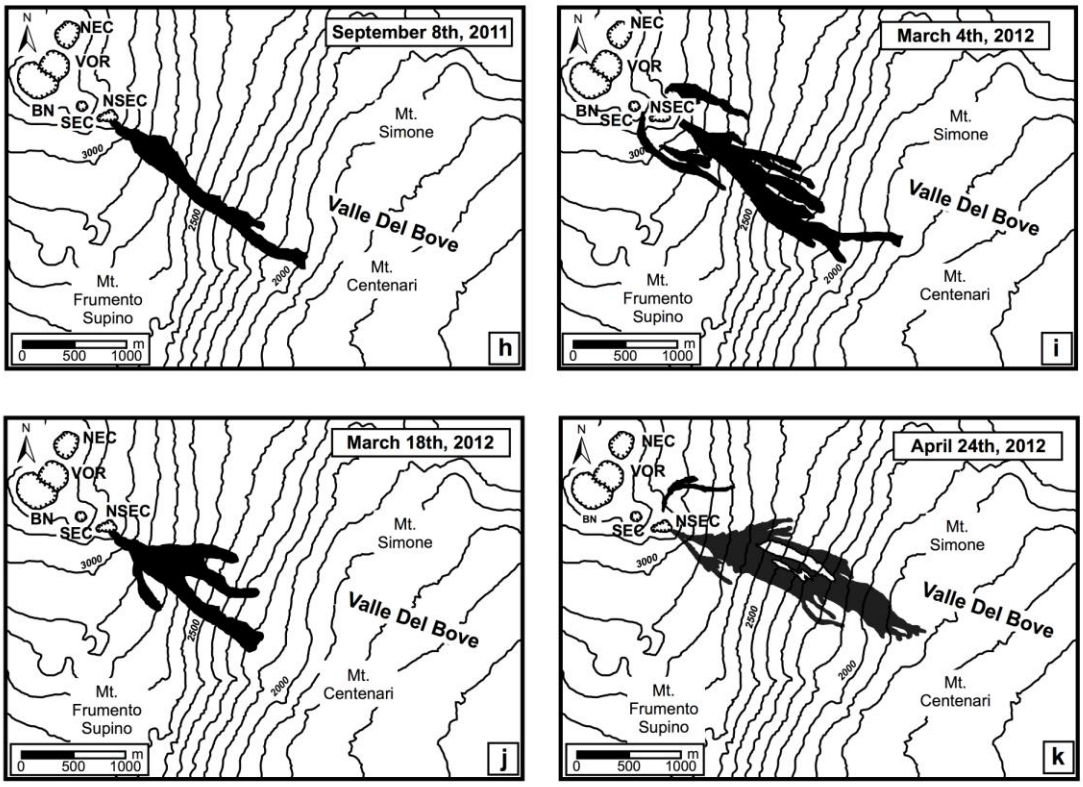

Figure 1 cont

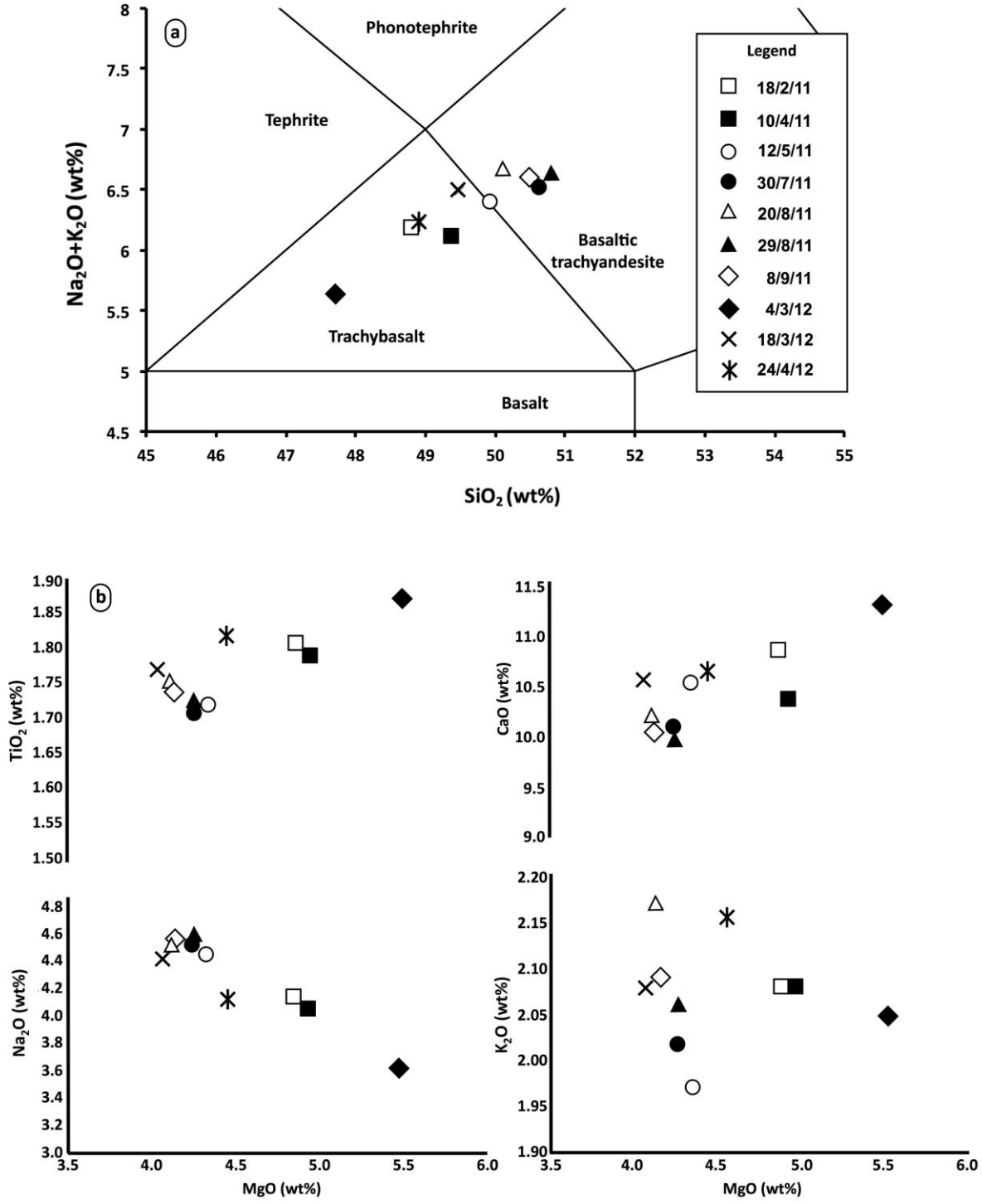

Figure 2

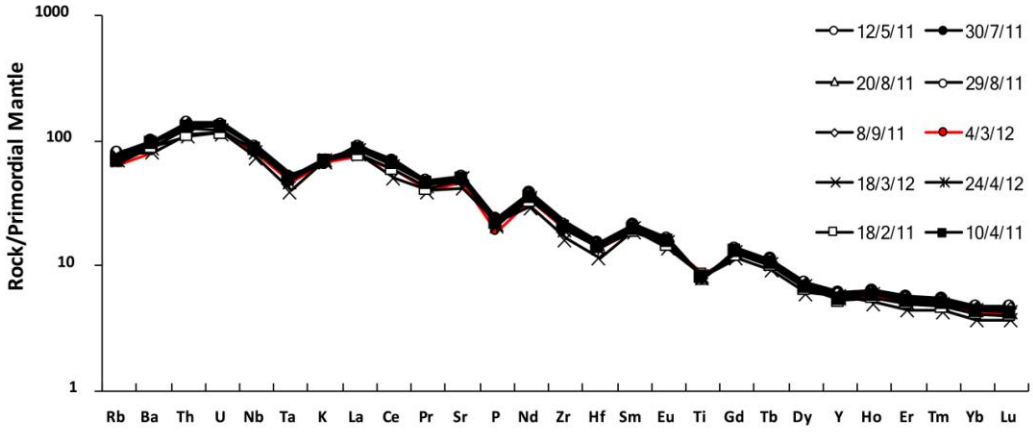

Figure 3

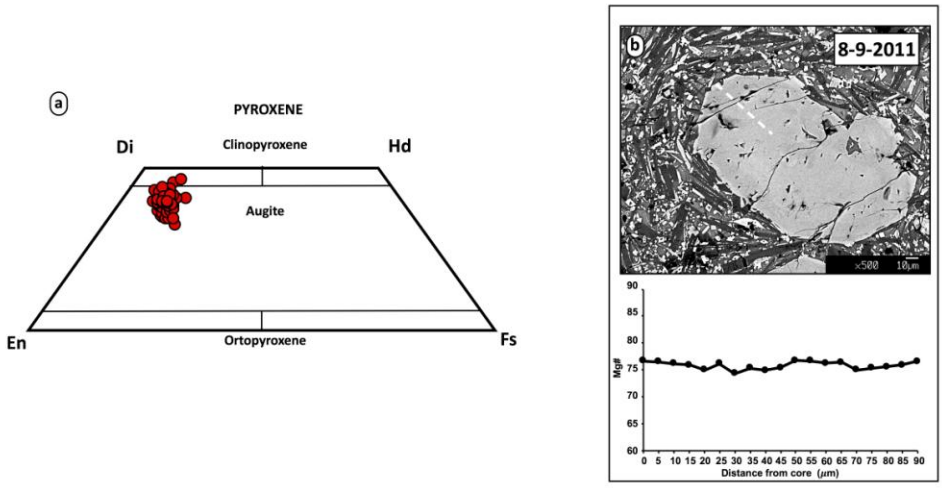

Figure 4

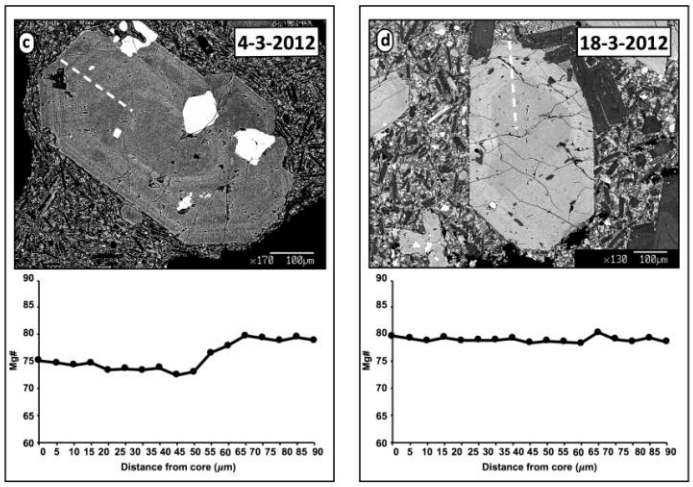

Figure 4 Cont

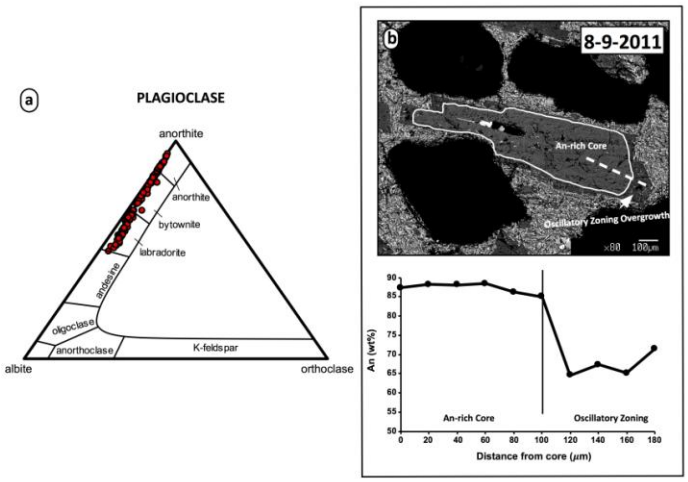

Figure 5

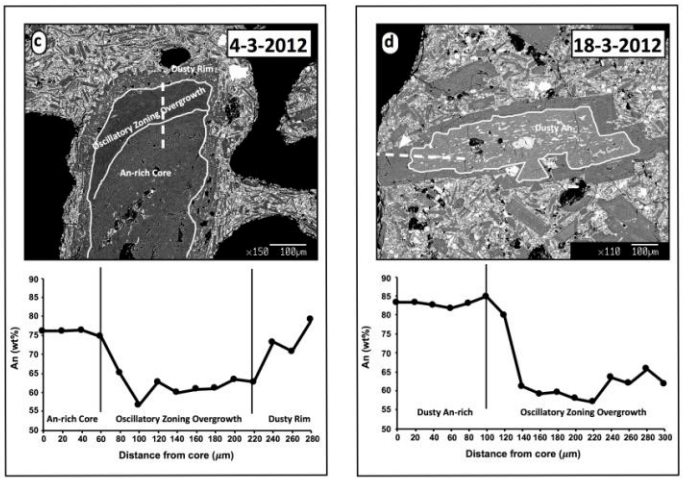

Figure 5 Cont

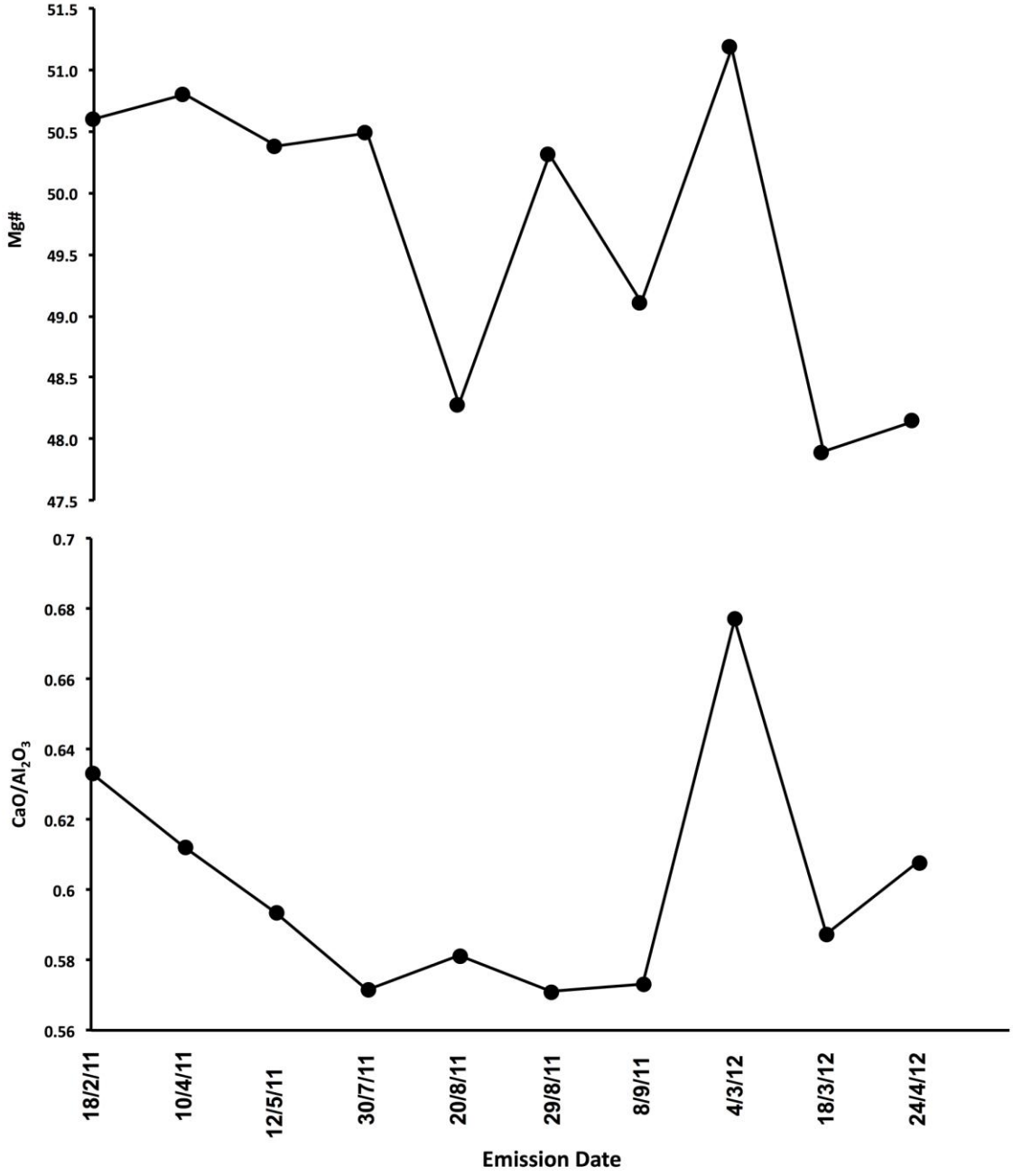

Figure 6

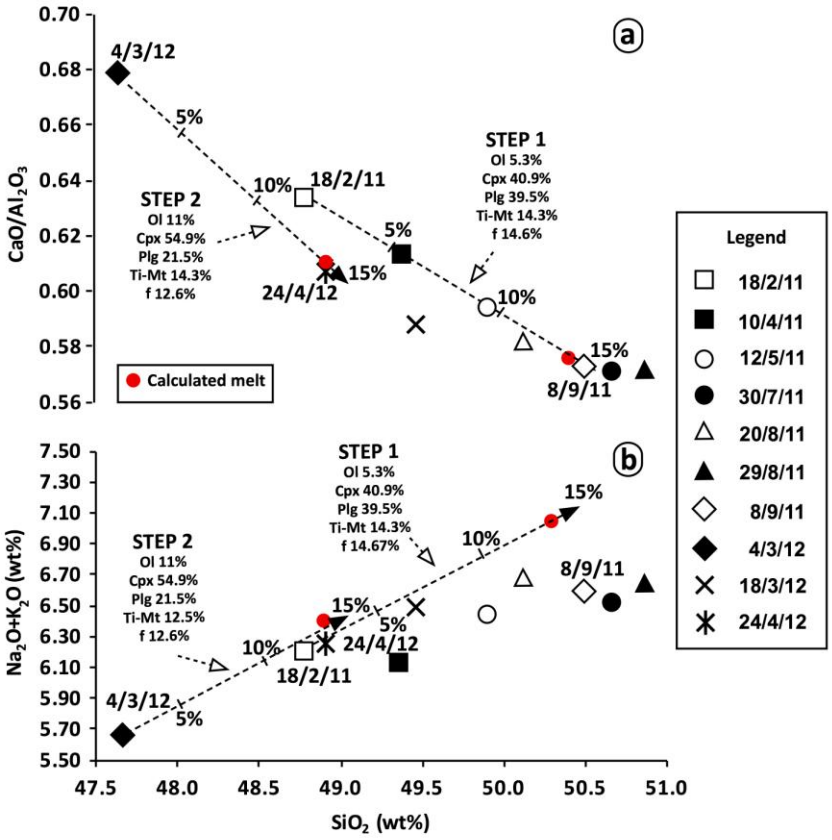

Figure 7

Figure 8

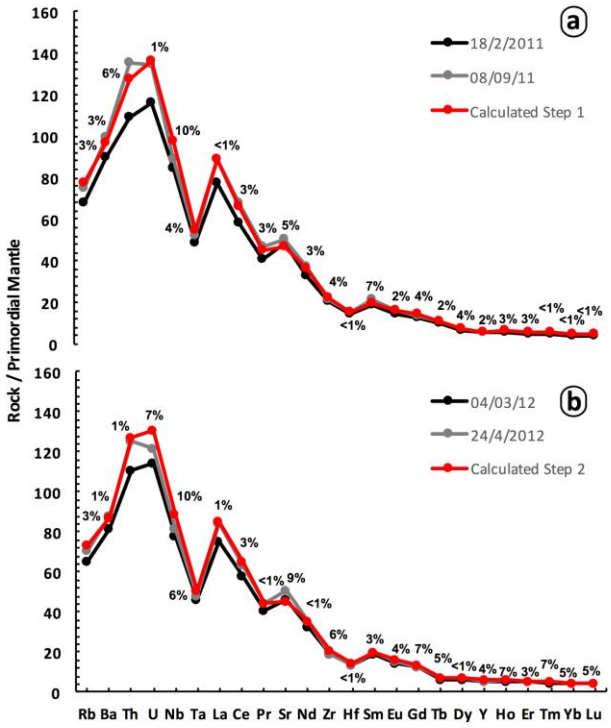

Figure 9

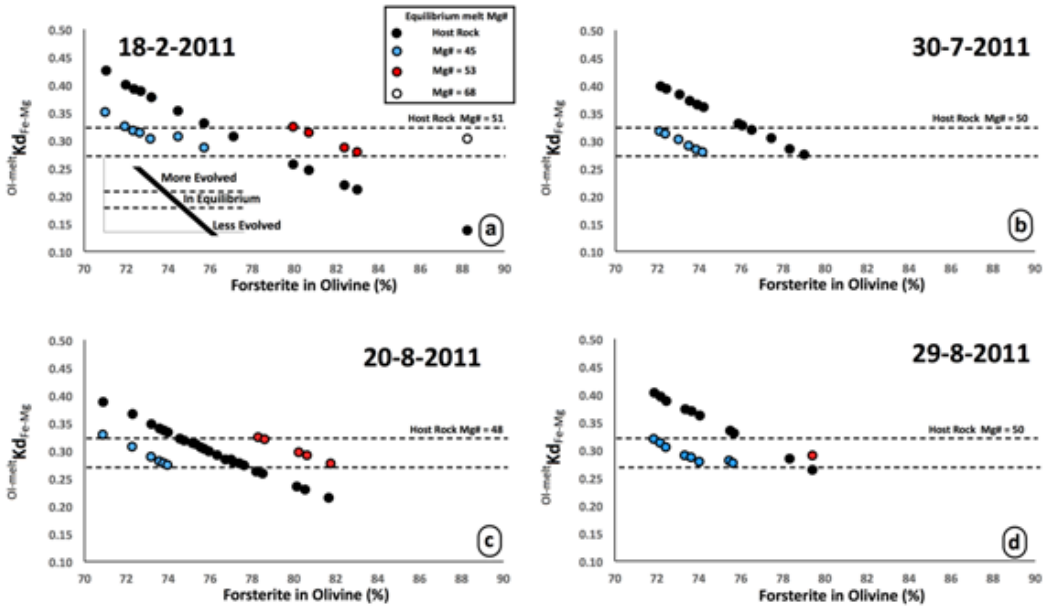

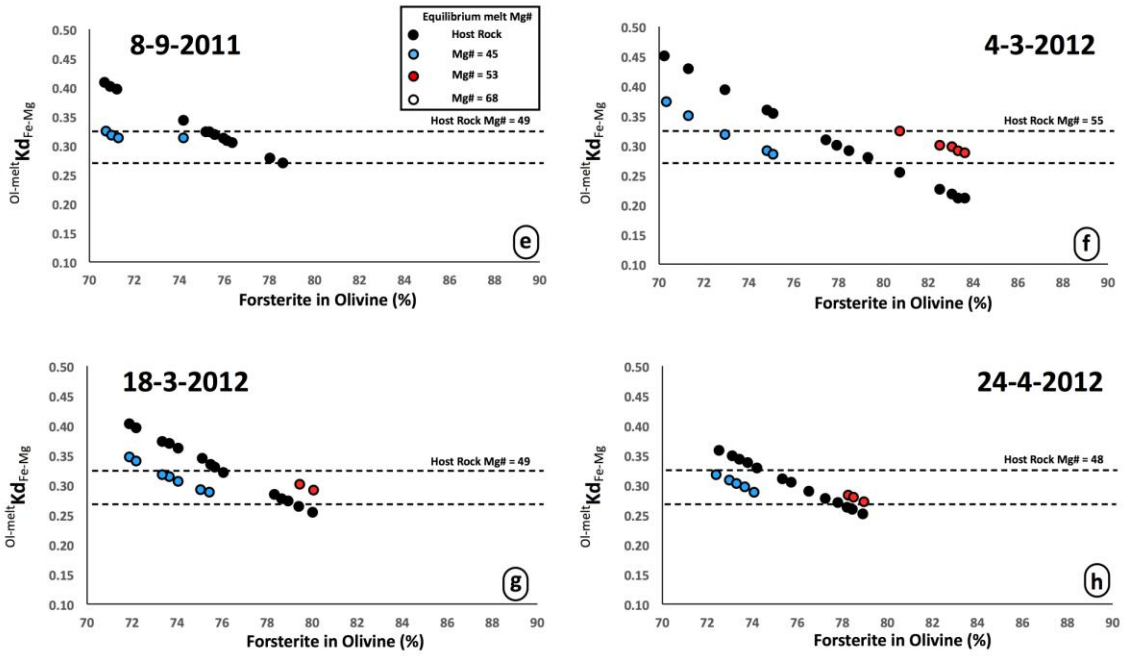

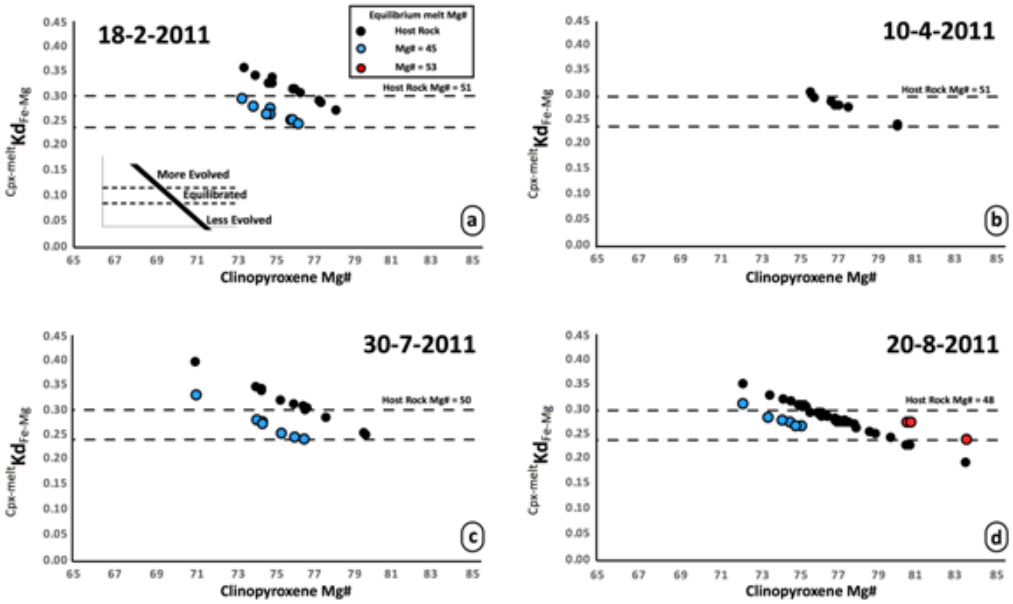

Figure 10

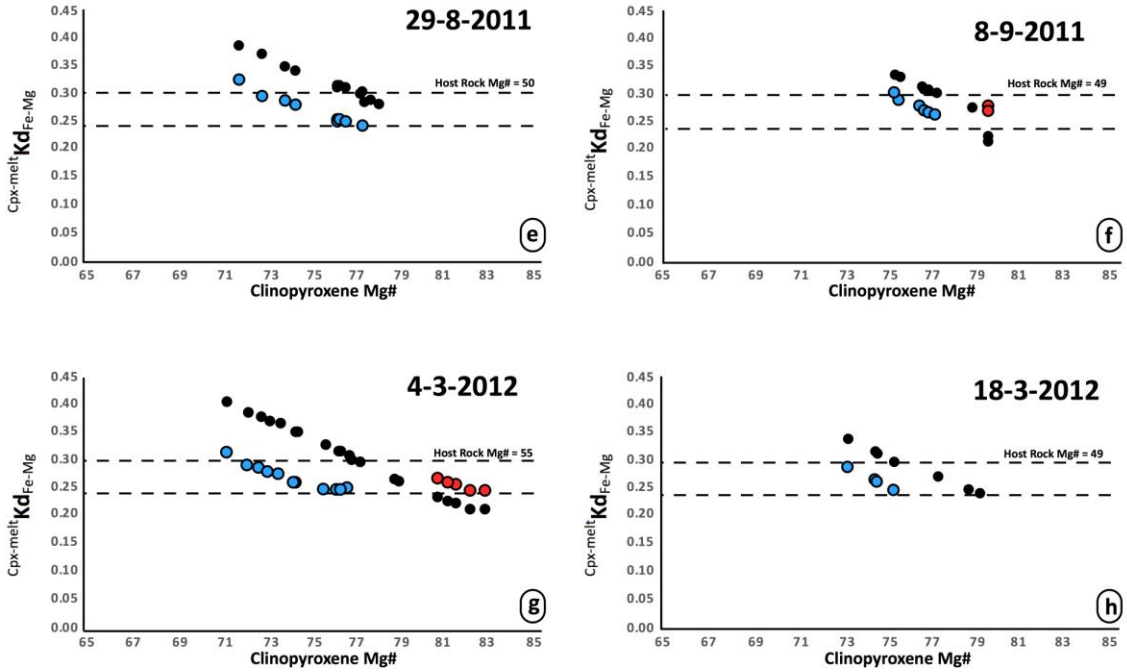

Figure 11

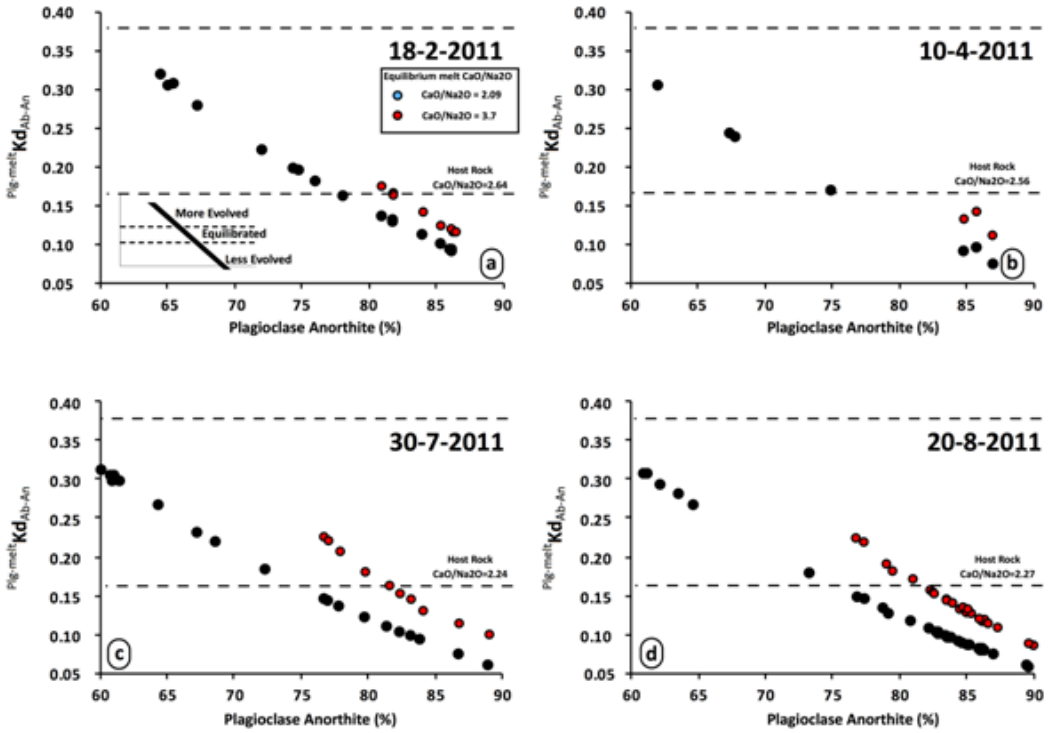

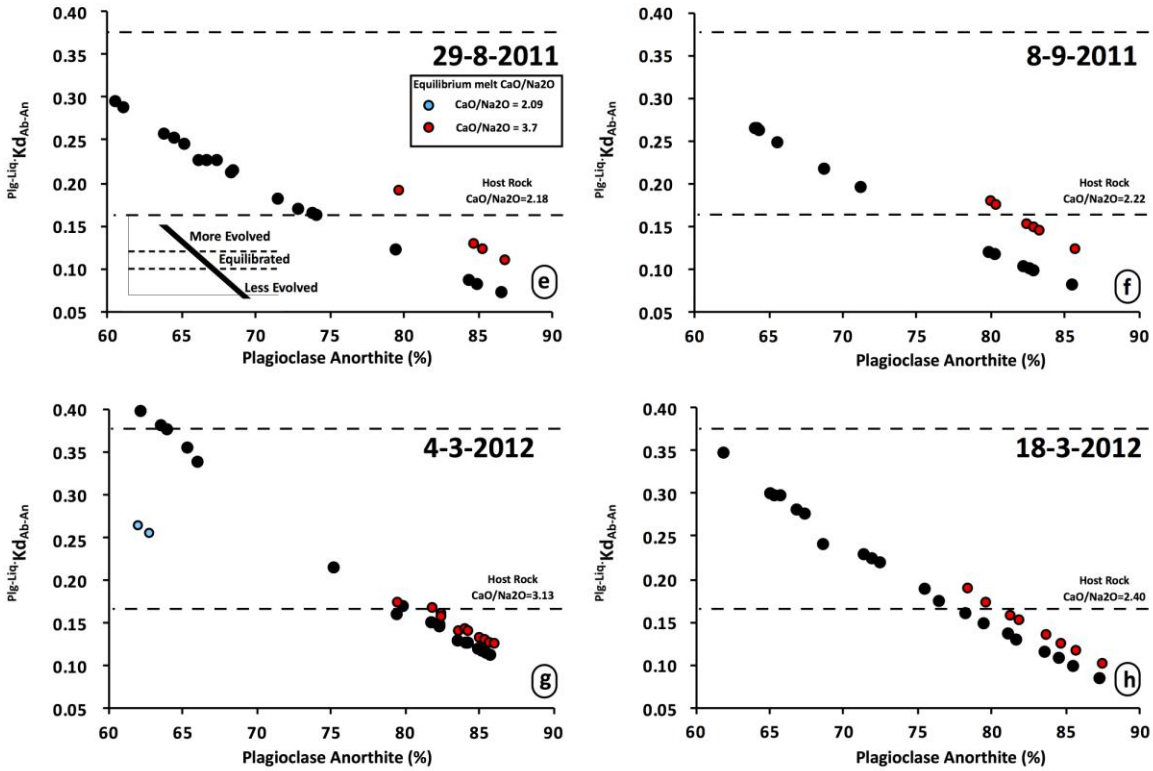

Figure 12

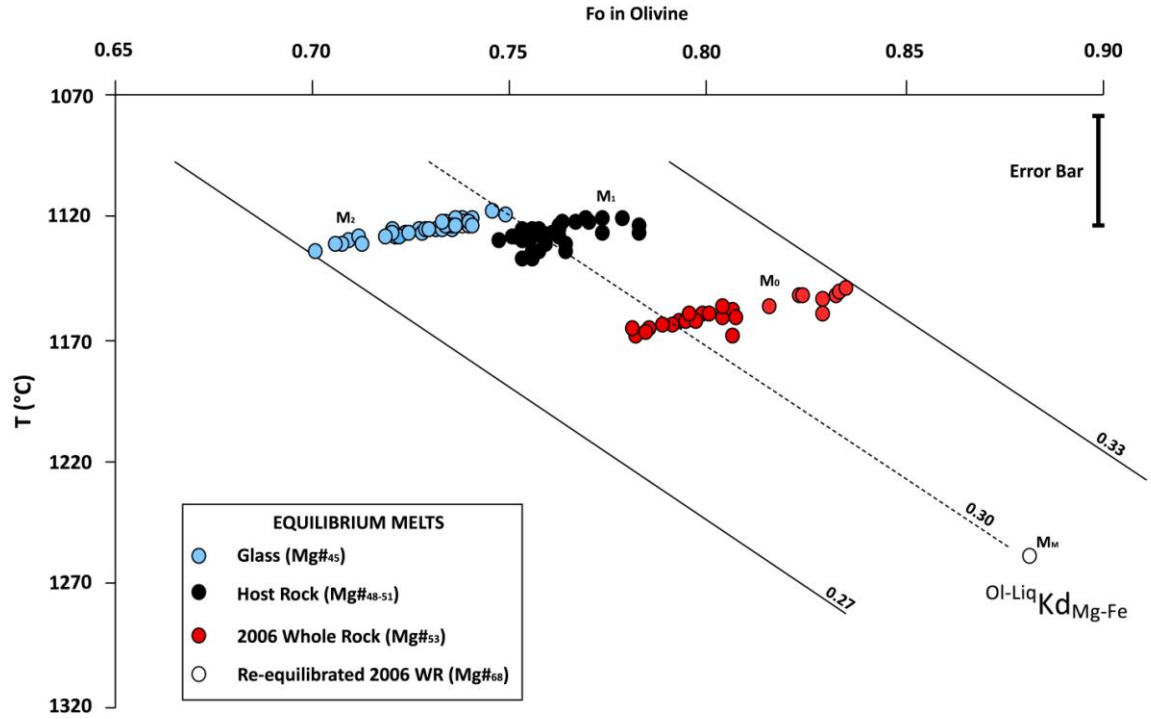

Figure 13

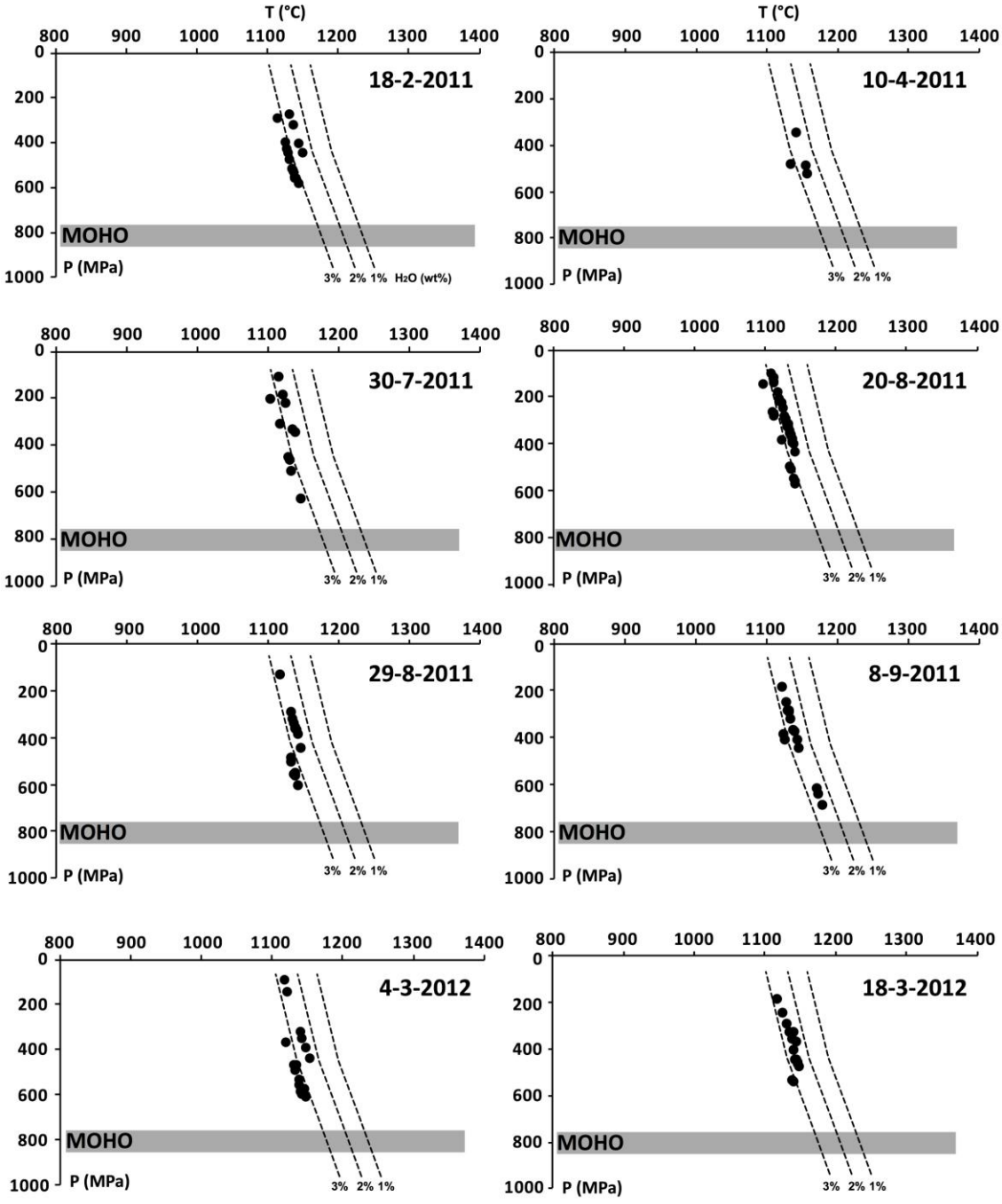

Figure 14

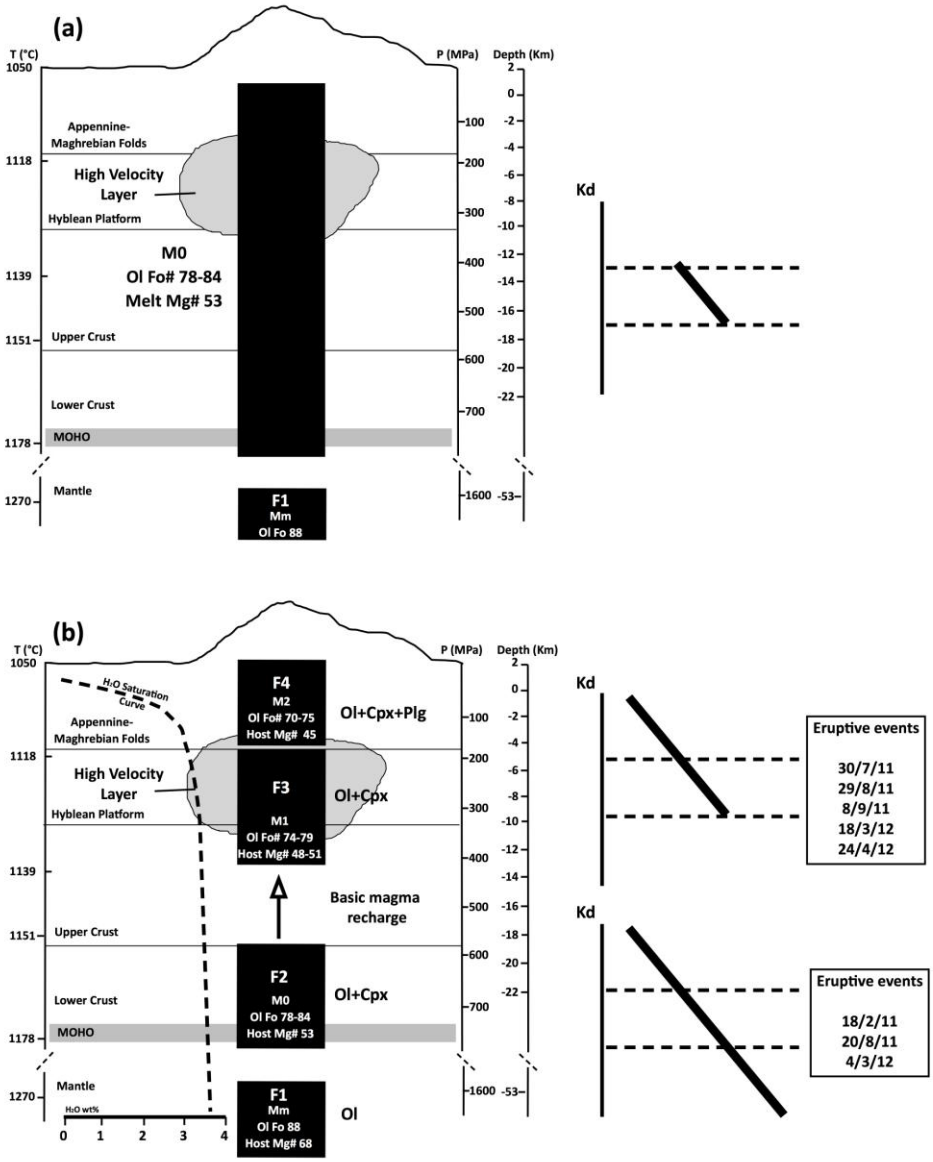

Date	Emission Vent	Type of activity	Start of paroxysmal phase(GMT)	End of paroxysmal phase (GMT)	Type of emitted products
12/1/11	South East Crater	Stromboli an	21:50	23:50	Scoriaceous lapilli
18/2/11	South East Crater	Stromboli an	03:30	12:30	Ashes and lapilli
10/4/11	South East Crater	Lava Fountain	08:05	13:30	Ashes and lapilli
12/5/11	South East Crater	Lava Fountain	02:20	05:00	Ashes and lapilli
9/7/11	South East Crater	Lava Fountain	13:45	14:45	Ashes and lapilli
19/7/11	South East Crater	Lava Fountain	00:05	02:30	Ashes and lapilli
24/7/11	South East Crater	Mixed	03:00	05:00	Ashes and lapilli
30/7/11	South East Crater	Lava Fountain	19:35	21:30	Ashes and lapilli
5/8/11	South East Crater	Lava Fountain	21:00	23:00	Ashes and lapilli
12/8/11	South East Crater	Mixed	08:30	10:00	Ashes and lapilli
20/8/11	South East Crater	Lava Fountain	07:00	07:30	Lava flows, ashes and lapilli
29/8/11	South East Crater	Mixed	04:05	04:45	Lava flows, ashes and lapilli
8/9/11	South East Crater	Lava Fountain	06:30	08:30	Ashes and lapilli
19/9/11	South East Crater	Lava Fountain	12:20	13:00	Ashes and lapilli
28/9/11	South East Crater	Lava Fountain	19:31	19:55	Ashes and lapilli
8/10/11	South East Crater	Lava Fountain	14:30	14:40	Ashes and lapilli
23/10/11	South East Crater	Lava Fountain	18:30	20:30	Ashes and lapilli
5/1/12	South East Crater	Mixed	05:00	06:50	Ashes and lapilli
9/2/12	South East Crater	Mixed	00:00	05:30	Ashes and lapilli
4/3/12	South East Crater	Mixed	07:30	09:32	Lava flows, ashes and lapilli
18/3/12	South East Crater	Mixed	08:00	09:45	Lava flows, ashes and lapilli
1/4/1	South East	Mixed	02:00	03:30	Ashes and lapilli

2	Crater				
12/4/	South East				
12	Crater	Mixed	14:30	15:15	Ashes and lapilli
24/4/	South East				Lava flows, ashes
12	Crater	Mixed	01:30	02:20	and lapilli

Table 1

Eruptive event	Phenocrysts (%)				Porphyritic Index (%)	Percentage of vescicules (%)	Type of Groundmass
	Ol	Cpx	Plg	Mt			
18/2/11	15	30	50	5	30	30	Glassy
10/4/11	<5	25	70	5	35	60	Glassy
12/5/11	<5	25	70	5	30	40	Hyalopilitic
30/7/11	10	35	60	5	30	60	Hyalopilitic
20/8/11	2	25	50	5	30	50	Hyalopilitic
29/8/11	10	30	55	5	30	40	Glassy
8/9/11	15	30	50	5	25-30	50	Glassy
4/3/12	30	40	25	5	15	60	Glassy
18/4/12	<5	25	65	5	25	50	Glassy
24/4/12	20	35	40	5	25	60	Glassy

Table 2

	18/2/11	10/4/11	12/5/11	30/7/11	20/8/11	29/8/11	8/9/11	4/3/12	18/3/12	24/4/12
SiO_2	48.78	49.36	49.91	50.63	50.10	50.82	50.48	47.69	49.46	48.91
TiO_2	1.81	1.79	1.71	1.71	1.75	1.72	1.73	1.87	1.76	1.82
Al_2O_3	17.16	16.97	17.74	17.65	17.53	17.41	17.54	16.70	17.97	17.52
FeO	8.30	8.36	7.46	7.28	7.70	7.34	7.50	9.17	7.73	8.38
Fe_2O_3	1.38	1.39	1.24	1.21	1.28	1.22	1.25	1.53	1.29	1.40
MnO	0.19	0.19	0.18	0.17	0.19	0.17	0.19	0.20	0.18	0.20
MgO	4.85	4.93	4.33	4.24	4.11	4.25	4.13	5.48	4.06	4.44
CaO	10.86	10.40	10.53	10.08	10.18	9.94	10.06	11.30	10.57	10.65
Na_2O	4.11	4.06	4.44	4.51	4.49	4.57	4.53	3.61	4.40	4.12
K_2O	2.08	2.08	1.97	2.01	2.17	2.05	2.09	2.06	2.09	2.12
P_2O_5	0.48	0.47	0.49	0.51	0.49	0.51	0.51	0.41	0.48	0.45
L.O.I.	0.42	0.35	0.30	0.37	0.22	0.44	0.47	0.40	0.31	0.33
Total	100	100	100	100	100	100	100	100	100	100
Mg#	50.91	51.14	50.73	50.85	48.64	50.66	49.42	51.50	48.24	48.48
Ca/Na	2.64	2.56	2.37	2.24	2.27	2.18	2.22	3.13	2.40	2.58
Sc	22.1	24.1	20.8	21.5	20	20.7	20.6	26.3	19.7	20.6
V	327	308	307	306	288	301	304	334	248	306
Ni	14.4	9.1	8.9	9.4	7.1	7.3	7.3	18.3	7.3	8.4
Co	40.9	37.1	37.2	35.7	35.5	36.1	33.3	39	32.8	38.2
Cr	46.3	31.6	34.8	35.9	32	30.4	35.7	52.4	24.1	32.3
Rb	43.2	44.0	44.8	49.4	49.6	52.1	47.5	41.6	48.6	45.3
Ba	625	671	668	702	675	698	697	572	566	619
Sr	1018	1031	1058	1078	1063	1114	1053	983	880	1069
Th	9.26	11.04	11.02	11.67	11.51	12.10	11.47	9.45	9.44	10.69
U	2.44	2.71	2.74	2.82	2.85	2.91	2.82	2.40	2.42	2.57
Hf	4.36	4.37	4.44	4.60	4.70	4.71	4.67	4.25	3.61	4.30
Zr	227	226	229	237	241	245	240	214	185	218

Ta	1.98	2.05	2.06	2.11	2.15	2.19	2.14	1.89	1.63	1.97
Nb	60.0	61.1	61.9	62.8	63.9	65.2	63.4	56.0	52.1	58.1
Y	23.9	24.8	25.2	27.3	25.8	27.6	26.3	24.2	26.3	25.8
La	53.4	59.5	59.2	61.6	59.8	63.7	61.2	52.0	53.4	57.9
Ce	103	117	117	121	119	113	121	104	89	112
Pr	11.3	12.4	12.4	13.0	12.6	13.3	12.9	11.2	11.1	12.2
Nd	44.7	48.6	48.5	51.1	49.4	52.2	50.6	44.8	39.9	48.3
Sm	8.34	8.78	8.88	9.43	8.97	9.53	9.31	8.44	8.43	9.00
Eu	2.48	2.62	2.62	2.75	2.63	2.79	2.72	2.50	2.34	2.63
Gd	7.35	7.72	7.75	8.14	7.82	8.30	8.06	7.42	6.86	7.79
Tb	1.08	1.13	1.14	1.21	1.14	1.22	1.18	1.10	1.01	1.15
Dy	4.84	5.05	5.09	5.42	5.18	5.46	5.33	4.95	4.46	5.17
Ho	0.91	0.96	0.96	1.03	0.99	1.04	1.02	0.93	0.83	0.98
Er	2.37	2.48	2.51	2.70	2.56	2.71	2.64	2.42	2.14	2.54
Tm	0.35	0.37	0.38	0.40	0.38	0.40	0.39	0.36	0.32	0.38
Yb	2.03	2.14	2.18	2.34	2.23	2.39	2.32	2.08	1.84	2.22
Lu	0.30	0.31	0.32	0.35	0.32	0.35	0.34	0.30	0.27	0.33

Table 3

MASS BALANCE FRACTIONATION RESULTS

	STEP 1 Starting Melt	Arrival Melt	Calculated Melt	
wt%	**18/2/2011**	**8/9/2011**		**Error (%)**
SiO_2	48.78	50.48	50.30	0.03
TiO_2	1.81	1.73	1.67	0.00
Al_2O_3	17.16	17.54	17.53	0.00
Fe_2O_3	0.00	0.00	0.00	0.00
FeO	9.55	8.62	8.56	0.00
MgO	4.85	4.13	4.16	0.00
CaO	10.86	10.06	10.18	0.02
Na_2O	4.11	4.53	4.61	0.01
K_2O	2.08	2.09	2.43	0.11
P_2O_5	0.48	0.51	0.56	0.00
Total	99.67	99.69	100.00	

	Fractionating Mass (%)	100% Norm
Ol	0.78	5.30
Cpx	6.00	40.90
Plg	5.79	39.50
Ti-Mt	2.10	14.30
f %	14.67	
r^2		**0.18**

	Starting 18/2/2011		Partition Coefficients (Kd)					Arrival 8/9/2011		
ppm	**C0**	**F**	**Ol**	**Cpx**	**Plg**	**Ti-Mt**	**D**	**Cl Calculated**	**Cl Measured**	**Error (%)**
Rb	43.2	0.86	0.0400	0.1300	0.3000	0.1100	0.19	49.3	47.5	3.76
Ba	625	0.86	0.0300	0.7440	0.5600	0.0003	0.53	675	697	-3.09
Th	9.26	0.86	0.0300	0.0400	0.0500	0.0005	0.04	10.8	11.5	-5.60
U	2.44	0.86	0.0400	0.0140	0.0600	0.0082	0.03	2.86	2.82	1.32
Nb	60.0	0.86	0.1100	0.1400	0.0100	0.1500	0.09	69.6	63.4	9.75
Ta	1.98	0.86	0.0300	0.0400	0.0400	1.7000	0.28	2.23	2.14	4.07
La	53	0.86	0.0300	0.2000	0.2000	0.0000	0.16	61.1	61.2	-0.16
Ce	103	0.86	0.0200	0.4800	0.1130	0.0001	0.24	117	120	-3.21
Pr	11.3	0.86	0.0000	0.7900	0.0630	0.0002	0.35	12.5	12.9	-2.76
Sr	1018	0.86	0.0200	0.1600	2.7000	0.0000	1.13	996	1053	-5.42
Nd	44.7	0.86	0.0023	1.0000	0.0690	0.0005	0.44	49.0	51.6	-3.02
Zr	227	0.86	0.0600	0.7900	0.1300	0.2900	0.42	249	239	4.12
Hf	4.36	0.86	0.0400	1.1000	0.0500	0.3800	0.53	4.71	4.67	0.94
Sm	8.34	0.86	0.0037	1.5100	0.3500	0.0006	0.76	8.68	9.31	-6.76
Eu	2.48	0.86	0.0300	0.3540	0.5000	0.0110	0.35	2.76	2.72	1.55
Gd	7.35	0.86	0.0168	0.4000	0.0260	0.0034	0.18	8.41	8.06	4.35
Tb	1.08	0.86	0.0300	0.7300	0.1000	0.0067	0.34	1.20	1.18	1.67
Dy	4.84	0.86	0.0263	1.5500	0.0190	0.0100	0.64	5.13	5.33	-3.82

Y	23.9	0.86	0.0090	0.6500	0.0080	0.0760	0.28	26.9	26.3	2.02
Ho	0.91	0.86	0.0016	0.3100	0.0480	0.0170	0.15	1.05	1.02	3.04
Er	2.37	0.86	0.0188	0.3126	0.0100	0.0000	0.13	2.73	2.64	3.46
Tm	0.35	0.86	0.0030	0.4490	0.0490	0.1000	0.22	0.40	0.39	0.83
Yb	2.03	0.86	0.0313	0.4300	0.0060	0.1700	0.20	2.31	2.32	-0.53
Lu	0.30	0.86	0.0383	0.2875	0.024	0.084	0.14	0.34	0.34	0.89

Table 4

	STEP 2 Starting Melt	Arrival Melt	Calculated Melt	
wt%	4/3/2012	24/4/2012		Error (%)
SiO_2	47.69	48.91	48.90	0.00
TiO_2	1.87	1.82	1.80	0.00
Al_2O_3	16.70	17.52	17.53	0.00
Fe_2O_3	0.00	0.00	0.00	0.00
FeO	10.54	9.63	9.71	0.01
MgO	5.48	4.44	4.47	0.00
CaO	11.30	10.65	10.73	0.01
Na_2O	3.61	4.12	4.05	0.00
K_2O	2.06	2.12	2.35	0.05
P_2O_5	0.41	0.45	0.47	0.00
Total	99.65	99.66	100.00	

	Fractionating Mass (%)	100% Norm
Ol	1.39	11.00
Cpx	6.93	54.90
Plg	2.72	21.55
Ti-Mt	1.58	12.52
f %	12.62	
r^2		**0.27**

	Starting 4/3/2012		Partition Coefficients (Kd)					Arrival 24/4/2012		
ppm	C0	F	Ol	Cpx	Plg	Ti-Mt	D	Cl Calculated	Cl Measured	Error (%)
Rb	41.6	0.87	0.0400	0.1300	0.3000	0.1100	0.19	46.6	45.3	2.96
Ba	572	0.87	0.0300	0.7440	0.5600	0.0003	0.53	611	619	-1.29
Th	9.45	0.87	0.0300	0.0400	0.0500	0.0005	0.04	10.8	10.7	1.05
U	2.40	0.87	0.0400	0.0140	0.0600	0.0082	0.03	2.75	2.57	7.27
Nb	56.0	0.87	0.1100	0.1400	0.0100	0.1500	0.09	63.6	58.1	9.32
Ta	1.89	0.87	0.0300	0.0400	0.0400	1.7000	0.28	2.09	1.97	6.26
La	52.0	0.87	0.0300	0.2000	0.2000	0.0000	0.16	58.4	57.9	1.00
Ce	104	0.87	0.0200	0.4800	0.1130	0.0001	0.24	115	112	2.57
Pr	11.2	0.87	0.0000	0.7900	0.0630	0.0002	0.35	12.3	12.2	0.71
Sr	983	0.87	0.0200	0.1600	2.7000	0.0000	1.13	965	1069	-9.72
Nd	44.8	0.87	0.0023	1.0000	0.0690	0.0005	0.44	48.5	48.3	0.38
Zr	214	0.87	0.0600	0.7900	0.1300	0.2900	0.42	232	218	6.19
Hf	4.25	0.87	0.0400	1.1000	0.0500	0.3800	0.53	4.54	4.30	5.60
Sm	8.44	0.87	0.0037	1.5100	0.3500	0.0006	0.76	8.73	9.00	-2.98
Eu	2.50	0.87	0.0300	0.3540	0.5000	0.0110	0.35	2.74	2.63	3.91
Gd	7.42	0.87	0.0168	0.4000	0.0260	0.0034	0.18	8.32	7.79	6.82
Tb	1.10	0.87	0.0300	0.7300	0.1000	0.0067	0.34	1.20	1.15	4.59
Dy	4.95	0.87	0.0263	1.5500	0.0190	0.0100	0.64	5.20	5.17	0.70
Y	24.2	0.87	0.0090	0.6500	0.0080	0.0760	0.28	26.8	25.8	3.89
Ho	0.93	0.87	0.0016	0.3100	0.0480	0.0170	0.15	1.05	0.98	6.95

Er	2.42	0.87	0.0188	0.3126	0.0100	0.0000	0.13	2.74	2.54	7.73
Tm	0.36	0.87	0.0030	0.4490	0.0490	0.1000	0.22	0.40	0.38	6.17
Yb	2.08	0.87	0.0313	0.4300	0.0060	0.1700	0.20	2.32	2.22	4.76
Lu	0.30	0.87	0.0383	0.2875	0.0240	0.0840	0.14	0.34	0.33	4.96

Table 5

	Matrix Glass	2006 Trachybasalt*	Equilibrated 2006**
SiO_2	50.38	47.94	47.22
TiO_2	2.11	1.82	1.61
Al_2O_3	16.66	18.07	15.54
FeO	8.09	8.47	7.36
Fe_2O_3	1.21	1.27	2.96
MnO	0.22	0.19	0.17
MgO	3.77	5.49	9.1
CaO	8.92	10.88	10.4
Na_2O	4.25	3.53	3.39
K_2O	3.4	1.9	1.85
P_2O_5	1.01	0.45	0.39
L.O.I.	0.3	0.26	-
Total	100.02	100.01	99.99
Mg#	45.37	53.53	68.71
Ca/Na	9.18	9.61	10.02

Table 6